Comparative Assessment of the Composition and Charge State of Nitrogenase FeMo-Cofactor

2 AUTHORS, INCLUDING:

Robert K Szilagyi

University of Pannonia, Veszprém

90 PUBLICATIONS   **2,661** CITATIONS

COMPARATIVE ASSESSMENT OF THE COMPOSITION AND CHARGE STATE OF NITROGENASE FeMo-COFACTOR

Travis V. Harris and **Robert K. Szilagyi**[*]
NAI Astrobiology Biogeocatalysis Research Center, Department of Chemistry and Biochemistry, Montana State University, Bozeman, MT 59717, United States

Abstract

A significant limitation in our understanding of the molecular mechanism of biological nitrogen fixation is the uncertain composition of the FeMo-cofactor (FeMo-co) of nitrogenase. In this study we present a systematic, density functional theory-based evaluation of spin coupling schemes, iron oxidation states, ligand protonation states, and interstitial ligand composition using a wide range of experimental criteria. The employed functionals and basis sets were validated with molecular orbital information from X-ray absorption spectroscopic data of relevant iron-sulfur clusters. Independently from the employed level of theory, the electronic structure with the greatest number of antiferromagnetic interactions corresponds to the lowest energy state for a given charge and oxidation state distribution of the iron ions. The relative spin state energies of resting and oxidized FeMo-co already allowed the exclusion of certain iron oxidation state distributions and interstitial ligand compositions. Geometry optimized FeMo-co structures of several models further eliminated additional states and compositions, while reduction potentials indicated a strong preference for the most likely charge state of FeMo-co. Mössbauer and ENDOR parameter calculations were found to be remarkably dependent on the employed training set, density functional and basis set. Overall, we found that a more oxidized $[Mo^{IV}-2Fe^{II}-5Fe^{III}-9S^{2-}-C^{4-}]$ composition with a hydroxyl-protonated homocitrate ligand satisfies all of the available experimental criteria, and is thus favored over the currently preferred composition of $[Mo^{IV}-4Fe^{II}-3Fe^{III}-9S^{2-}-N^{3-}]$ from the literature.

1. Introduction

Biological nitrogen fixation is catalyzed by the two-component nitrogenase metalloenzyme.[1] The catalytically active [M-7Fe-9S] cluster of nitrogenase is present in three forms distinguished by its composition, where M is Mo, V or Fe. The Mo-containing nitrogenase is the most active and the most studied, and thus is the focus of this research. A significant limitation in understanding the molecular basis of biological nitrogen fixation is the lack of electronic structural and compositional knowledge of the catalytically active iron-molybdenum-sulfur cluster cofactor, FeMo-co. FeMo-co has been identified as a

[Mo-7Fe-9S-X] cluster from the nearly atomic resolution (1.16 Å) crystal structure of the MoFe protein of nitrogenase.[2] While the composition of the central ligand (X) could not be

[*]Author to whom correspondence should be addressed at Szilagyi@Montana.EDU .

unambiguously established experimentally, the crystallographic analysis of the resolution-dependent electron-density profile and the interaction of nitrogenase with dinitrogen and ammonia suggested that X is likely N. The two neighboring elements also fit well the experimental electron density profiles. In FeMo-co, these atoms would correspond to carbido (C^{4-}), nitrido (N^{3-}), or oxo (O^{2-}) ligands. Other 10 electron ions as alternative ligands, such as B^{5-}, F^-, Na^+, or Mg^{2+} can likely be excluded due to charge incompatibility (see below) or limited biochemical availability (B^{5-}, F^-). The Cys275 and His442 residues at the terminal Fe and Mo, respectively, and a non-protein ligand, homocitrate, complete the FeMo-co inner sphere coordination environment.

The MoFe-protein has been isolated with three forms of FeMo-co: resting or native (FeMo-co^N), one-electron reduced (FeMo-co^{Red}) and one-electron oxidized (FeMo-co^{Ox}).[3] Electron nuclear double resonance (ENDOR) data suggest the Mo center is diamagnetic with a formally +IV ($4d^2$) oxidation state in the resting form.[4] X-ray absorption spectroscopic (XAS) measurements further support the presence of Mo^{IV} oxidation state in all three forms.[5, 6] FeMo-co^N shows a characteristic $S_t = 3/2$ EPR signal, while the reduced form is EPR silent with integer spin, $S_t \geq 1$. The oxidized form is diamagnetic as observed at 4 K,[7-9] but a low lying excited $S_t \geq 1$ state is populated between 240 and 320 K.[10] The reduction potential for the FeMo-co^{Ox}/FeMo-co^N couple has been determined to be -42 mV,[11] while the second reduction step for FeMo-co^N/FeMo-co^{Red} has only been estimated to be -465 mV.[3]

FeMo-co can be extracted (exFeMo-co) into N-methyl formamide (NMF) solution with the homocitrate ligand remaining coordinated, a deprotonated solvent anion (NMF$^-$) substituting the negatively charged thiolate of Cys275, and a neutral NMF molecule replacing the imidazole of His442.[12] A cation binding study indicated that exFeMo-co^{Ox} has an overall charge of -2.[13] With a plausible assumption that the protonation state of homocitrate is the same in the protein-bound and extracted form, the charge of FeMo-co^{Ox} can be considered to be the same as the exFeMo-co^{Ox}. Thus, the charge of FeMo-co^N can be assigned to -3, which provides a criterion for evaluating the formal oxidation states of the unknown Fe centers. Moreover, the $S_t = 3/2$ resting form and a diamagnetic Mo^{IV} center limit the formal Fe oxidation states to $6Fe^{II}$-$1Fe^{III}$, $4Fe^{II}$-$3Fe^{III}$, $2Fe^{II}$-$5Fe^{III}$, and a $7Fe^{III}$ state that is unlikely due to the required Fe^{IV} site in the oxidized form within a sulfide coordination environment. ^{57}Fe ENDOR experiments led to the suggestion of the $6Fe^{II}$-$1Fe^{III}$ assignment for the CO-bound FeMo-co,[14] while Mössbauer isomer shifts were more consistent with the $4Fe^{II}$-$3Fe^{III}$ state for the resting form.[15] An electrochemical study of exFeMo-co linked the above Mössbauer and ENDOR assignments by implying that the CO-bound form is more consistent with a 2-electron reduced form relative to the resting state.[12]

Earlier computational studies employing density functional theory (DFT) have also favored the $4Fe^{II}$-$3Fe^{III}$ oxidation state for the resting form. Vrajmasu *et al.* calculated Mössbauer isomer shifts for all possible Fe oxidation states and X = C^{4-}, N^{3-}, and O^{2-}; only the $[4Fe^{II}$-$3Fe^{III}$-$N^{3-}]$, $[4Fe^{II}$-$3Fe^{III}$-$C^{4-}]$, and $[2Fe^{II}$-$5Fe^{III}$-$N^{3-}]$ oxidation state assignments were consistent with experiments.[16] An indication for the interconnectedness of the formal oxidation states of the Fe centers and the nature of the interstitial ligand was already found by Lovell *et al.*, who initially obtained computational results preferring the $6Fe^{II}$-$1Fe^{III}$ state using an early FeMo-co model without the presence of an interstitial atom.[17] However, inclusion of an anionic central ligand gave better agreement between the calculated and experimental Mössbauer isomer shifts for the $[4Fe^{II}$-$3Fe^{III}$-$N^{3-}]$ state than that of $[6Fe^{II}$-$1Fe^{III}$-$N^{3-}]$.[18] Furthermore, structural optimizations favored the $4Fe^{II}$-$3Fe^{III}$ state with either N^{3-} or C^{4-} while disfavoring O^{2-}. The calculated reduction potentials indicated that $[4Fe^{II}$-$3Fe^{III}$-$N^{3-}]$ was the most likely oxidation state and composition. Notably, the

results for the $[2Fe^{II}\text{-}5Fe^{III}\text{-}N^{3-}]$ state/composition was not reported. By comparing HOMO energies of FeMo-co and Fe-S clusters, Dance found preference for $[4Fe^{II}\text{-}3Fe^{III}\text{-}N^{3-}]$, or $[4Fe^{II}\text{-}3Fe^{III}\text{-}C^{4-}]$ with a protonated μ^2-sulfide or Fe site.[19, 20] Comparison of the three lowest energy spin states showed that $[2Fe^{II}\text{-}5Fe^{III}\text{-}N^{3-}]$ had an $S_t = 3/2$ ground state, consistent with experiment, while $[4Fe^{II}\text{-}3Fe^{III}\text{-}N^{3-}]$ had an $S_t = 5/2$ ground state. The $S_t = 3/2$ state was found to be about 20 kJ/mol higher for the latter. By contrast, using non-collinear spin calculations, Shimpl *et al.* reported $S_t = 3/2$ to be the ground state for $[4Fe^{II}\text{-}3Fe^{III}\text{-}N^{3-}]$, while the ground states for $[2Fe^{II}\text{-}5Fe^{III}\text{-}N^{3-}]$ and $[6Fe^{II}\text{-}1Fe^{III}\text{-}N^{3-}]$ were $S_t = 1/2$ and $S_t = 0.24$, respectively, with the optimized $[4Fe^{II}\text{-}3Fe^{III}\text{-}N^{3-}]$ giving the best agreement with experiment.[21] In summary, previous computational work favors the $[4Fe^{II}\text{-}3Fe^{III}\text{-}N^{3-}]$ state, although other states and compositions could not be unequivocally ruled out.

It is important to note that density functional theory calculations can be greatly influenced by the nature of exchange and correlation functionals, the amount of mixing of exact exchange, the completeness of employed basis sets, and the level of truncation of the employed computational model. In addition, due to the presence of high spin Fe centers within weak-field ligand environments, the method of describing ferro- and antiferromagnetic interactions is critical. Mössbauer[15] and ENDOR[22] measurements indicate four parallel spins and three antiparallel to the majority spin (spin-up or α) direction. While theoretically not exact,[23] a commonly used practical method to treat spin coupling interaction within the formalism of DFT is the broken symmetry (BS) approach.[24] For FeMo-co[N], Noodleman defined 10 major BS spin-coupling patterns[17] with numerous alternative spin-configurations. In addition to the challenge of obtaining and maintaining the correct spin state, the lowest energy BS state was found to depend on the chemical composition of the computational model and the employed density functional.[25] As discussed below, the atomic coordinates of computational models are also critical, particularly when the coordinates are based on a protein crystal structure with modest resolution. Furthermore, the protonation states of coordinated residues and ligands are often unknown, even for a close to atomic resolution protein structure. The protonation state of the homocitrate ligand is a key aspect that has not yet been systematically evaluated. This is important, since as a charged ligand, the homocitrate contributes to the overall charge of FeMo-co. Furthermore, the protonation state can also affect the bonding interactions around the Mo center and thus have implications for a proposed mechanism in which homocitrate becomes monodentate, opening up a coordination site for N_2.[26] 2 The deprotonated homocitrate ligand with a charge of −4 (or a truncated version with a charge of −2) has been chosen for many theoretical studies,[18, 20, 27, 28] while some assume a −3 charge for the complete ligand.[14, 16] An earlier computational work already suggested the possibility that the coordinated hydroxyl oxygen is protonated in the resting form.[29] Others proposed that protonation of the coordinated carboxylate group may be the first step of the catalytic mechanism.[26, 30]

In this study we carried out a comprehensive evaluation of a comprehensive compilation of experimental data with respect to spin coupling schemes, spin state energies, iron oxidation states, compositions of the interstitial atom, protonation states of the coordinated groups of the homocitrate ligand, reduction potentials, isomer shifts, quadrupole splittings and hyperfine coupling parameters. Based on a series of structural, energetic, electronic, and magnetic criteria, we can rule out certain compositions and oxidation states, and we find that only the $[Mo^{IV}\text{-}2Fe^{II}\text{-}5Fe^{III}\text{-}9S^{2-}\text{-}C^{4-}]^+$ composition with hydroxyl-protonated homocitrate ligand (HC^{3-}) is favored consistently for FeMo-co[N].

2. Computational Details

The computational model of FeMo-co (Figure 1) was based on the highest resolution

(1.16 Å) crystal structure of the MoFe protein available to date from *Azotobacter vinelandii* (PDB ID 1M1N)[2]. The ligands Cys275, His442, and homocitrate were truncated to methylthiolate, imidazole, and glycolate, respectively. We consider glycolate to be an acceptable computational model of homocitrate for evaluating the electronic and geometric structures of FeMo-co due to the limited role of the omitted distal carboxylate arms of homocitrate in polarization of the FeMo-co electron density similarly to weakly bound, solvated counter ions. The majority of this work (see below for exceptions) was carried out using Gaussian03 Rev. E.01[31] employing the gradient-corrected Becke88[32] exchange and Perdew86[33] correlation functionals (BP86) and the Stuttgart-Dresden effective core potentials and valence basis set (SDD-VTZ(d))[34-36] for all atoms, with additional polarization functions for Fe[37], Mo[37] and S[38]. This choice was rigorously validated for [4Fe-4S] clusters in a previous work,[39] and to ensure consistency, representative calculations (see below) were also carried out with hybrid functionals such as B3LYP[40], B(5HF)P86[41] and/or a larger basis set (6-311+G(d))[42]. Isomer shifts, quadrupole splittings and the hyperfine coupling constant for interstitial ligand X were calculated using ADF2009[43-45] at the BP86/STO-TZP level, with an integration accuracy of 5. The Conductor like Screening Model (COSMO)[46-49] with $\varepsilon = 30$ was used to approximate the polar environments of the complexes in the isomer shift training set, while the less polar constant, $\varepsilon = 10$, was used to approximate the dielectric environment of the protein matrix around FeMo-co. The spin coupling calculations were all carried out using the oxidation state assignment and composition [4Fe^{II}-3Fe^{III}-N^{3-}] on the experimental FeMo-co structure for *in vacuo* computational models. Notably, gas phase calculations for models with −4 or greater negative overall charge showed unreasonable spin densities; thus, these highly charged models were embedded in a polarizable continuum model (PCM)[50-52] with $\varepsilon = 10$. Relative energies of spin states calculated using PCM were within 2 kJ/mol of corresponding energy differences from gas phase calculations. However, for consistency, all geometry optimizations were performed in the presence of PCM. Optimizations at the computationally more expensive B(5HF)P86/6-311+G(d) level resulted in geometric structural deviations of only 0.01 Å relative to BP86/SDD-VTZ(d). This is similar to previously determined experimental vs. calculated structural differences of less than 0.03 Å (RMS value) for the model system, [Fe$_4$S$_4$(SEt)$_4$]$^{2-}$ at B(5HF)P86/6-311+G(d) level.[39]

Ferro- and antiferromagnetic spin coupling schemes were obtained using the broken symmetry (BS)[24] approach.[53] The initial localized spin states were constructed by the ionic fragment approach.[39] For example, the FeMo-co^{Ox} state has been described in the literature as diamagnetic ($S_t = 0$).[7-9] Thus, the initial electronic structure was constructed from Fe^{II} ($m_s = \pm2$) and Fe^{III} ($m_s = \pm5/2$) centers to result in an $M_s = 0$ state, where the total number of spin up (α) and spin down (β) electrons was equal. Consistently we use the S_t and M_s spin quantum numbers to differentiate among the pure spin states and the calculated broken symmetry (BS) spin states. The initial ionic electronic structure was allowed to relax to the broken-symmetry solution. The order of Fe^{II} and Fe^{III} centers in the ionic fragments had no effect on the converged broken-symmetry state. Pure antiferromagnetically coupled spin states were considered for reduction potential calculations by using a spin projection procedure[54] based on the Heisenberg Hamiltonian with FeMo-co modeled as a two spin-system. This approach is conceptually incorrect due to the presence of 7 paramagnetic centers; however, this can be considered as a first order approximation due to the formal topology of FeMo-co being composed of a [Mo-3Fe-3S] and a [4Fe-3S] clusters that are coupled through three bridging sulfide and the central ligands. With this simplified model, there is a linear relationship between energies and expectation values of the spin operator

($<S^2>$), which was determined from the broken symmetry and the pure ferromagnetically coupled (maximal S_t) state. Then the energy of the pure ground spin state was obtained using the known $<S^2>$-value (e.g., 15/4 for an $S_t = 3/2$ state). A more rigorous approach to spin projection,[55] in which the Hamiltonian included coupling between the individual Fe sites, was carried out for $[4Fe^{II}\text{-}3Fe^{III}\text{-}N^{3-}]$, and the projected ground state energy only deviates by 4 kJ/mol between the two approaches (see Section 3.2). Double exchange[56] effects were not included in the spin state analysis due to technical limitations. These are the subject of ongoing work, as an extensive treatment adds substantial complexity, even to two-center systems, such as [2Fe-2S] clusters.[57] A recent work considered double exchange interactions for a multinuclear spin system on top of the Heisenberg exchange and an effective Coulomb intercenter repulsion;[58] however, due to computational limitations the size of the system was limited to six Fe.

In order to evaluate the adequacy of the selected level of theory, the comparison of experimental[59] and calculated sulfur 3p orbital characters (S(3p)) of metal-sulfide bonds was carried out. Sulfur K-edge X-ray absorption spectroscopic measurements[59] for a prototypical model complex of $[Fe_4S_4(SEt)_4]^{2-}$ define a total of 1.23 and 0.41 e donation from the bridging sulfides and thiolate sulfurs to the irons. The theoretical sulfur covalency values were derived from the difference between the S(3p) atomic populations of the covalent electronic structure and the theoretical ionic limit of six electrons. S(3p) characters were obtained from the Natural Population Analysis (NPA)[60] with a minimal valence set, where S(3d), Fe(4s, 4p), Mo(5p) and higher orbitals were treated as part of the Rydberg atomic orbital set. The BP86/SDD-VTZ(d) level gives 1.19 and 0.40 e S(3p) character for the Fe-sulfide and Fe-thiolate bonds that already well approximate the experimental values. Employing a larger all-electron basis set (6-311+G(d)) and an experimentally validated hybrid functional, B(5HF)P86,[41] improve only slightly this agreement to 1.22 and 0.42 e. A detailed analysis of errors in calculated parameters for the same model system has already been published.[39]

To determine reduction potentials that include contributions from solvation effects, free energy changes ($\Delta G°_{reduction}$) were calculated[61] according to the following equations:

$$\Delta G°_{reduction} = \Delta G°_{solute} + \Delta\Delta G°_{solvation} \tag{1}$$

$$\Delta G°_{solute} = \Delta\varepsilon_{SCF}^{s.p.} + \Delta ZPE_{solute,corr} + \Delta H°_{solute,corr} - T\Delta S°_{solute,corr} \tag{2}$$

$$\Delta\Delta G°_{solvation} = \Delta\Delta G_{electrostatic} + \Delta\Delta G_{nonelectrostatic} \tag{3}$$

where $\Delta\varepsilon_{SCF}^{s.p.}$ is the difference in the gas phase spin projected (indicated by the superscript 's.p.') ground state electronic energy of the PCM-optimized reduced and oxidized forms. The enthalpy, entropy and zero-point energy (ZPE) corrections were calculated as changes between the reduced and oxidized forms of the solute; $\Delta G_{electrostatic}$ refers to the electrostatic solute-solvent interactions; and $\Delta G_{nonelectrostatic}$ refers to the non-electrostatic cavitation, dispersion and repulsion energies of solvent-solvent interactions. Overall, in this approach we take into account both inner and outer sphere relaxation effects including the geometric relaxations upon solvation. The standard one-electron reduction potentials ($n = 1$) were then calculated using the Nernst equation:

$$\Delta G^{\circ}{}_{\mathrm{reduction}} = -nFE^{\circ} \tag{4}$$

where F is the Faraday constant, 23.06 kcal mol^{-1} V^{-1}. A -4.43 eV correction was applied as a reference for the absolute reduction potential of the normal hydrogen electrode (NHE).[11] The use of only gas phase optimized structures and exclusion of the corrections due to geometric changes upon solvation can introduce a considerable 60 mV error.[62] With the above approach, the gas phase optimizations actually can be omitted, since each contribution mentioned in Equations (1)-(3) can be derived from PCM-optimized structures and related energy analysis.

Mössbauer quadrupole splittings, ΔE_{Q}, were calculated from the electric field gradient tensors (V) in a coordinate system where $V_{zz} \geq V_{xx} \geq V_{yy}$, using Eq. (5), where e is the elementary charge, Q is the nuclear quadrupole moment of ^{57}Fe (0.158 barn)[63] and η is the asymmetry parameter ($|V_{xx}-V_{yy})/V_{zz}|$).

$$\Delta E_{\mathrm{Q}} = \frac{1}{2} e Q V_{zz} \sqrt{1 + \frac{\eta^2}{3}} \tag{5}$$

Hyperfine coupling constants (HFCC) depend critically on the spin-polarized electron density at the nucleus ($\rho_s(0)$), which is difficult to calculate accurately for transition metal systems.[64] For multinuclear complexes, magnetic interactions and the use of the BS approach further complicate the calculations. Neese $et\ al.$ have developed a method based on the Heisenberg Hamiltonian,[65] which derives scaling factors for calculated HFCCs at transition metal centers. However, a recent study of the [6Fe-6S] catalytic cluster of [FeFe]-hydrogenase demonstrates that even with the scaling factors the absolute accuracy of calculated HFCCs is low, although the ratios of HFCCs can be qualitatively useful.[66] In this work we employ a semi-empirical method developed by Mouesca $et\ al.$,[67, 68] which avoids calculation of the problematic $\rho_s(0)$ values. The procedure has previously been used to analyze spin coupling in FeMo-co[17] and the P-cluster[67] of nitrogenase.

The isotropic contributions to the observed HFCCs (a_i^{exp}) for Fe sites in a spin coupled system are proportional to the projections (K_i) of the local site spins (S_i) onto the total spin. Thus, the hyperfine parameters (a_i^{calc}) were determined using the following equation:

$$a_i^{\mathrm{calc}} = K_i \left(|\rho_s(\mathrm{Fe}_i)| / 2S_i \right) a_i^{\mathrm{ionic}} \tag{6}$$

In Equation (6), the spin densities, $\rho_s(\mathrm{Fe}_i)$, scale the empirically derived[68] intrinsic Fe site parameters, a_i^{ionic}, which are -34.0 MHz, -32.5 MHz, and -31.0 MHz for Fe^{2+}, Fe$^{2.5+}$ and Fe^{3+} with $S_i = 2$, 9/4 and 5/2, respectively. K_i factors (see Table S12) were calculated according to Eq. (7) developed by Noodleman and coworkers.[17, 25]

$$K_i = \langle \boldsymbol{S}_i \cdot \boldsymbol{S}_t \rangle / \langle \boldsymbol{S}_t \cdot \boldsymbol{S}_t \rangle \tag{7}$$

Calculations of hyperfine couplings for X = ^{14}N or ^{13}C were also performed according to Eq. (8) by Noodleman and coworkers,[25] where $a_{\mathrm{iso}}^{\mathrm{BS}}(\mathrm{X})$ values were obtained from the broken symmetry calculation and scaled by the P_{x} factors 0.40, 0.46 and 0.51 for the 6Fe$^{\mathrm{II}}$-1Fe$^{\mathrm{III}}$, 4Fe$^{\mathrm{II}}$-3Fe$^{\mathrm{III}}$ and 2Fe$^{\mathrm{II}}$-5Fe$^{\mathrm{III}}$ oxidation state distributions, respectively.

$$a_{\text{iso}}(X) = \frac{1}{6} \sum_{i=2,3...7} (|K_i/S_i|S_t) \, a_{\text{iso}}^{\text{BS}}(X) = P_X a_{\text{iso}}^{\text{BS}}(X)$$

(8)

Due to the local symmetry of the central 6 Fe belt and the bridging sulfide ligands, we considered the same hyperfine coupling interaction between the Fe and the interstitial atom, X. The electron density at X takes into account the individual effects of the neighboring Fe sites, and the projection of the calculated hyperfine coupling of X onto the total spin $S_t = 3/2$ takes into account the individual projection coefficients and spin of each Fe site.

The ^{57}Fe isomer shifts (δ) from Mössbauer spectroscopy are directly proportional to the electron density at the nuclei, $\rho(0)$. Calculated $\rho(0)$ values are dependent on the employed functional and basis set;[69] thus, to calculate the ^{57}Fe isomer shifts for FeMo-co, the relationship between $\rho(0)$ and δ was obtained for a training set, which is composed of [Fe-S] and [Mo-Fe-S] clusters of various charge and spin states. The calculated and experimental values were fit to Eq. (9), where a constant, A (in $e \, a_0^{-3}$), was chosen to reduce the magnitude of $\rho(0)$ (in $e \, a_0^{-3}$), and the fit parameters are α (in $e^{-1} \, a_0^3 \, \text{mm s}^{-1}$) and C (in mm s^{-1}).

$$\delta = \alpha \, (\rho(0) - A) + C$$

(9)

3. Results and Discussion

3.1 Evaluation of Broken-Symmetry Spin Coupling Schemes

Assuming weak-field ligand environments from the thiolate and sulfide ligands, the formally Fe$^{\text{III}}$ and Fe$^{\text{II}}$ centers adopt high-spin $S = 5/2$ and 2 states, respectively. The total spin ($S_t = 3/2$) of FeMo-co^N is a result of ferro- and antiferromagnetic coupling between the Fe centers, of which four have parallel and three have antiparallel (4+3) spin orientations according to the interpretations of ENDOR[22] and Mössbauer[15] data. When FeMo-co's electronic structure is treated with broken symmetry (BS) formalism, a given charge and oxidation state distribution with high-spin Fe centers can have 35 nonequivalent BS states with $M_s = 3/2$ that are also consistent with the above-mentioned experimental 4+3 spin orientation. These states can be divided into 10 groups based on the number of antiferromagnetically coupled Fe pairs. The first type is bridged by two sulfides, and the second bridged by one sulfide and X (see representative states in Figure 2A).[17] The former is exclusive to pairs that include the terminal Fe. There is a third type of Fe pair, which is bridged by only X. In order to build up a reference base for *a priori* choosing the lowest energy spin state, we evaluated all 35 spin states (see Table S1). We also evaluated the dependence of the relative energies of spin coupling states on the applied functional (BP86 vs. B3LYP) and basis set (SDD-VTZ(d) vs. 6-311+G(d)).

Figure 2 summarizes the results obtained for the relative energies of various spin-coupling schemes of [4Fe$^{\text{II}}$-3Fe$^{\text{III}}$-N^{3-}].[70] The results in Figure 2A display a trend of lower energy with increasing numbers of sulfide-bridged antiferromagnetically coupled pairs of Fe centers ($N_{Fe-S-Fe}$) at the BP86/SDD-VTZ(d) level. Representative individual coupling schemes within each of the 10 major groups are depicted in the inset of Figure 2A. Notably, the BS2 state is strikingly (>25 kJ/mol) lower in energy than the BS9 and BS5 states, even though they all have the same $N_{Fe-S-Fe}$ (6). This is because BS2 has an additional six X-bridged antiferromagnetically coupled Fe pairs ($N_{Fe-X-Fe}$), while BS9 and BS5 have four. Similarly, BS4 and BS10 are almost equivalent in energy to BS8 and BS6 because the former ones have more $N_{Fe-S-Fe}$ (8 vs. 7), but less $N_{Fe-X-Fe}$ (4 vs. 6). Thus, the primary factor affecting

the stability of BS states is the number of individual M-L-M antiferromagnetic interactions ($2N_{Fe-S-Fe} + N_{Fe-X-Fe}$), as shown in Figure 2B.

Figure 2C shows a representative state for each number of antiferromagnetically coupled Fe pairs calculated at the different levels of theory (see Table S2 for numerical results). Although the overall trend is the same in each case, there is a notable functional dependence for the order of higher lying states in Figure 2C. With the pure DFT (GGA) functional, BP86, the lowest energy spin state other than BS7 in Figure 2C is BS6, consistent with the findings of Noodleman and coworkers,[25] who examined the same representative states using a GGA functional, PW91. However, we find that using the popular hybrid functional, B3LYP, BS10 is lower in energy than BS6. Most importantly, the ground state for each evaluated level of theory is BS7, and the overall trend is the same. A similar trend was also observed by Noodleman and coworkers using an early FeMo-co model without the interstitial atom, although BS6 was found to be the ground state.[17] With $X = N^{3-}$ and a change in functional, they found BS7 to be the ground state for $X = N^{3-}$,[25] in agreement with results from Blöchl and coworkers,[21] who used a different theoretical approach. Additionally, ESEEM and ENDOR measurements indicate that if $X = N$ or C the hyperfine coupling to X is weak, which, as shown by DFT, favors a spin state with symmetric spins in the central '6Fe-belt', such as BS7.[25]

Within BS7, the oxidation states $6Fe^{II}$-$1Fe^{III}$, $4Fe^{II}$-$3Fe^{III}$ and $2Fe^{II}$-$5Fe^{III}$ can be described by several formal distributions that all satisfy $M_s = 3/2$. Three such distributions are given for the $2Fe^{II}$-$5Fe^{III}$ state in Figure 3. Although the formal subcluster M_s values vary, due to delocalization, calculations converge to a single electronic structure (Figure 3, far right). Thus, the cluster oxidation state, M_s value and spin coupling scheme are enough to uniquely describe an electronic structure, without specifying the specific oxidation state distribution.

3.2 Spin State Dependence on Oxidation States and Compositions for FeMo-co^N and FeMo-co^{Ox}

A commonly considered criterion for evaluating the likeliness of a given oxidation state and composition for FeMo-co is that the ground spin state must be consistent with the experimentally observed $S_t = 3/2$. It is important to realize that the consideration of only weak-field, high spin Fe^{II} and Fe^{III} centers limits the possible oxidation states of the resting form to $6Fe^{II}$-$1Fe^{III}$, $4Fe^{II}$-$3Fe^{III}$ $2Fe^{II}$-$5Fe^{III}$, and $7Fe^{III}$, all of which can access the $S_t = 3/2$ state. The $7Fe^{III}$ state is unlikely, as discussed in the introduction, and was not considered here. In order to assess the ground and excited spin states, the energies of $S_t = 5/2$ and $1/2$ states for each oxidation state with $X = C^{4-}$, N^{3-} or O^{2-} were compared to $S_t = 3/2$ using the lowest energy BS7 spin coupling scheme with high spin Fe^{III} and Fe^{II} centers at atomic coordinates derived from the crystal structure[2]. Due to the limitation of the BS approach, only the M_s value is defined in the FeMo-co calculations.[53]

The relative spin state energies presented in this section have been calculated by assuming that the BS7 state with a given M_s value best represents the spin state of corresponding S_t, i.e., the $S_t = 3/2$ state is modeled by an $M_s = 3/2$ BS state. To estimate the validity of this assumption we have considered the Heisenberg spin Hamiltonian. As a first order approximation, FeMo-co can be considered as a two spin system, where a single exchange coupling constant, J, couples the [4Fe-3S] subcluster to the [Mo-3Fe-3S] subcluster. With this model, the spin projected[54] ground state is −22 kJ/mol lower in energy than the ground BS state for [$4Fe^{II}$-$3Fe^{III}$-N^{3-}], and excited spin states are similarly corrected by about −20 kJ/mol. Thus the two-spin model will not effect the relative ordering of the ground and the closest BS state energies. As an improvement to the single J model, the coupling of all 7 spin sites with 18 J constants was carried out using the Yamaguchi generalized spin projection method,[55] and spin state energies were obtained by diagonalizing a sizeable

Hamiltonian.[71] For [4Fe^{II}-3Fe^{III}-N^{3-}] oxidation/composition the resulting ground state remains $S_t = 3/2$ and it is 18 kJ/mol lower in energy than the $M_s = 3/2$ BS7 state. The lowest energy $S_t = 1/2$ and $S_t = 5/2$ states lie about 5 kJ/mol above the ground $S_t = 3/2$ state. Overall, the BS and the Heisenberg approaches both give qualitatively correct results with respect to the experimental $S_t = 3/2$ ground state, and the same relative ordering of excited states. Furthermore, from a through analysis of the eigenvectors of the Heisenberg Hamiltonian we find that the BS7 state with high spin Fe centers and a particular M_s value ($\pm 3/2$, for example) has the highest weighing (11%) among all of the more than 10000 BS states in the lowest energy pure spin state with a corresponding S_t value (3/2, accordingly).

In contrast to other work,[19, 21] Figure 4A shows that $M_s = 3/2$ is the lowest lying BS state regardless of the oxidation state and composition. The preferred 4Fe^{II}-3Fe^{III} assignment has a large energy gap (> 30 kJ/mol) between the ground and excited spin states; this becomes considerably less (~10 kJ/mol) for 6Fe^{II}-1Fe^{III} and 2Fe^{II}-5Fe^{III}. Overall, an $M_s = 3/2$ ground state does not allow for discriminating between compositions, charges, or formal oxidation states (for numerical results see Table S3).

The oxidized form of FeMo-co (FeMo-co^{Ox}) has an even electron $S_t = 0$ ground spin state according to Mössbauer[7, 8] and MCD[9] measurements, providing another means of evaluating oxidation state and composition. The energies of three spin states, $M_s = 0$, 1, or 2, were calculated for the 5Fe^{II}-2Fe^{III}, 3Fe^{II}-4Fe^{III} and 1Fe^{II}-6Fe^{III} oxidation states, which are the corresponding one-electron oxidized forms of 6Fe^{II}-1Fe^{III}, 4Fe^{II}-3Fe^{III}, and 2Fe^{II}-5Fe^{III} (with an $S_t = 3/2$ ground state), respectively. As shown in Figure 4B, when using the FeMo-co^N crystal structure for oxidized calculations, no combination of Fe centers and interstitial atom has an $M_s = 0$ ground state. Importantly, using structurally optimized FeMo-co^{Ox} models, we find that the $M_s = 0$ state becomes the ground spin state for 1Fe^{II}-6Fe^{III} (Figure 4C) with a low lying $M_s = 1$ state (~3 kJ/mol), showing a close agreement with experiment[10]. For 3Fe^{II}-4Fe^{III} and 5Fe^{II}-2Fe^{III}, geometry optimized structures show the same experimentally inconsistent high energy $M_s = 0$ state as in Figure 4B (for numerical results see Table S4). However, if the 3Fe^{II}-4Fe^{III} state is considered to be the reduced form of 2Fe^{II}-5Fe^{III}, rather than the oxidized form of 4Fe^{II}-3Fe^{III}, then the results are consistent with the $S_t \geq 1$ state shown by experiment. Independently from the composition of the interstitial atom, these results indicate a strong preference for the 1Fe^{II}-6Fe^{III} oxidation state assignment for FeMo-co^{Ox}, which in turn corresponds to 2Fe^{II}-5Fe^{III} for the resting FeMo-co^N form.

3.3 Geometric Differences with Various Oxidation States and Compositions

As shown for the relative energies of FeMo-co^{Ox} spin states, electronic structure is intimately linked to geometric structure. Comparison of the interatomic distances in selected optimized FeMo-co^N structures to those in the nearly atomic resolution (1.16 Å) crystal structure[2] and Extended X-ray Absorption Fine Structure analyses[6, 72] can provide another criterion for evaluating different compositions, charges and iron oxidation state distributions, as these properties are expected to affect the overall size of the cluster and the Fe-X bond lengths. Table 1 compares the structural optimization results for the FeMo-co^N form in the most probable states, [2Fe^{II}-5Fe^{III}-N^{3-}], [2Fe^{II}-5Fe^{III}-C^{4-}], [4Fe^{II}-3Fe^{III}-O^{2-}], [4Fe^{II}-3Fe^{III}-N^{3-}], and [4Fe^{II}-3Fe^{III}-C^{4-}], with experimental metric data. The optimized structure of the [2Fe^{II}-5Fe^{III}-O^{2-}] state is not reported here due to cluster dissociation. The results for the [6Fe^{II}-1Fe^{III}-N^{3-}] state are shown in Table S5, but this is unlikely relevant due to its highly reduced state. Looking at the S(Cys)-Fe through Fe$^{(Fe)}$···Fe$^{(Fe)}$ distances, the 2Fe^{II}-5Fe^{III} structures are generally contracted by up to 0.07 Å relative to the crystal structure, while the 4Fe^{II}-3Fe^{III} structures are expanded up to 0.07 Å. Notable exceptions are the Fe$^{(Fe)}$···Fe$^{(Fe)}$ distances in [4Fe^{II}-3Fe^{III}-O^{2-}], which are 0.14 Å expanded. The Fe$^{(Fe)}$···Fe$^{(Fe)}$ distances are expected to be among the most sensitive to the composition of

X, along with the $Fe^{(Fe)}$-X, $Fe^{(Fe)}\cdots Fe^{(Mo)}$, $Fe^{(Mo)}\cdots Fe^{(Mo)}$ and $Fe^{(Mo)}$-X distances. For X = O^{2-}, these distances are 0.10 Å – 0.16 Å expanded relative to the crystal structure compared to deviations of −0.02 Å – 0.06 Å for X = N^{3-} and C^{4-}. The stronger donation from the higher charged and less electronegative N^{3-} or C^{4-} interstitial atoms seems to be necessary to maintain short distances between X and the Fe centers.[73] Similar to previous studies,[18, 25, 74] we find that O^{2-} is likely not the interstitial atom based on geometric criteria. At this level of experimental information and theoretical treatment, the differences between the structures with N^{3-} *versus* C^{4-} are too small (less than 0.03 Å) to be able to unambiguously rule out either composition.

In the [Mo-3Fe-3S] subcluster there are modest contractions and expansions of 0.02 Å in the $Fe^{(Mo)}$-$S^{(b)}$ bond length for the $2Fe^{II}$-$5Fe^{III}$ and the $4Fe^{II}$-$3Fe^{III}$ structures, respectively. These trends reverse for the $Fe^{(Mo)}\cdots Fe^{(Mo)}$ distances, which are about 0.05 Å longer in $2Fe^{II}$-$5Fe^{III}$ than in the $4Fe^{II}$-$3Fe^{III}$ structures or crystal structure. The remaining distances in the Mo-containing subcluster ($Fe^{(Mo)}\cdots Mo$, $S^{(Mo)}$-$Fe^{(Mo)}$, and $S^{(Mo)}$-Mo) are 0.04 Å to 0.09 Å expanded relative to the experimental structures regardless of the composition and oxidation state. The core metrics without the terminal ligand distances have acceptably low overall RMS deviations of 0.04 Å – 0.05 Å for FeMo-co^N relative to the experimental structures; however, the [Mo-3Fe-3S] subcluster expands in $4Fe^{II}$-$3Fe^{III}$ and $2Fe^{II}$-$5Fe^{III}$, while the [4Fe-3S] subcluster expands in $4Fe^{II}$-$3Fe^{III}$ structure, but contracts in $2Fe^{II}$-$5Fe^{III}$. The end-to-end distance of FeMo-co (Fe$\cdots$Mo) shows a large difference. In $4Fe^{II}$-$3Fe^{III}$, the longest dimension of the cluster is at least 0.17 Å expanded, while in $2Fe^{II}$-$5Fe^{III}$, this distance deviates by only 0.01 Å from the experimental value of 7.00 Å. The significance of the 0.17 Å expansion may be limited by considering the percent difference from 7.00 Å, yet the preference of the Mo^{IV}-$2Fe^{II}$-$5Fe^{III}$ assignment for FeMo-co^N cannot be ignored, since the magnitude of this deviation is considerable larger than the uncertainty in the crystallographic coordinates at 1.16 Å resolution.

As proposed earlier,[2, 18] we also considered protonated interstitial ligands, such as HN^{2-}, HC^{3-} and H_2C^{2-} ions, for the $2Fe^{II}$-$5Fe^{III}$ oxidation state. When X = HC^{3-}, the Fe centers closest to the H atom on the interstitial ligand are repelled, resulting in overall expansion of the cluster. The average and RMS deviations are very similar (0.11 Å) to those observed for X = O^{2-} composition. The expansion is more extreme with HN^{2-} and H_2C^{2-} due to considerably reduced *e* donation to the Fe centers and, in the case of H_2C^{2-}, the larger size. On the basis of these structural findings, we can rule out protonated interstitial ligands as filling the central cavity of FeMo-co.

3.4 The Protonation State of the Homocitrate Ligand

A large deviation of 0.15-0.22 Å from the experimental structure is found between the Mo center and the $O_{hydroxyl}$ group of the homocitrate ligand (Table 1 - columns marked with OH for the homocitrate hydroxyl group, $HC(O_{hydroxyl})$, vs. experimental values). This is an important difference, because the protonation state of this ligand can significantly affect the electronic structure and thus the redox and coordinative properties of the Mo site. Due to lack of a strong secondary coordination sphere effect involving this hydroxyl group, the long experimental Mo-$O_{hydroxyl}$ bond indicates that the hydroxyl arm of the homocitrate is likely protonated. To test the correlated effects of ligand protonation and coordination geometry, a set of structural optimizations was carried out for the $[2Fe^{II}$-$5Fe^{III}$-$N^{3-}]$ state in which either the uncoordinated δ-N of imidazole was deprotonated (imidazolato ligand) or the glycolate ligand was protonated at the proximal carboxyl oxygen, the distal carboxyl oxygen or the hydroxyl oxygen. The variations in the Mo$\cdots$Fe and Mo-L distances are summarized in Table 2. The presence of an imidazolato ligand results in a slight increase of the Mo-O bond lengths; however, the Mo-N bond length becomes unreasonably short (2.17 Å) relative to the experimental values of 2.30 Å (crystallography) and 2.29 Å (EXAFS). Protonation of

either oxygen atoms of the carboxyl group results in an expanded $Mo-O_{carboxyl}$ bond (2.26 and 2.24 Å) without significantly improving the $Mo-O_{hydroxyl}$ bond length (2.01 Å). However, the hydroxyl-protonated model, $Mo-O_{hydroxyl}$, shows excellent agreement with the crystallographic data (both 2.20 Å). Furthermore, the $Mo\cdots Fe$ and $Mo-S$ distances decrease by 0.03-0.04 Å to 2.74 and 2.37 Å, respectively, which are closer to the crystallographic values (2.69 and 2.34 Å) than in the deprotonated form. As expected, the conjugate $Mo-O_{carboxyl}$ and $Mo-N(His)$ bonds to the $Mo-O_{hydroxyl}$ bond decrease by 0.02-0.03 Å to compensate for the decreased donation from $O_{hydroxyl}$ to the Mo center compared to the deprotonated model. However, this decreases the level of agreement in these bond lengths relative to the crystal structure to 0.10 and 0.09 Å, respectively. Overall, the improved $Mo\cdots Fe/Mo-S$ distances and the good agreement in the $Mo-O_{hydroxyl}$ bond length favor the $O_{hydroxyl}$-protonated homocitrate ligand model with an RMS deviation of 0.06 Å compared to 0.12 Å without protonation relative to the crystal structure. We rationalize the disagreement in other Mo-ligand bond lengths by the absence of second sphere coordination sphere interactions in our computational model, such as a network of hydrogen bonded water molecules around the coordinated short carboxyl arm of the homocitrate[29, 75-77] and the εN of His442.

Using the $O_{hydroxyl}$-protonated state, the best agreement with experimental data is achieved for the $[2Fe^{II}-5Fe^{III}-C^{4-}]$, $[4Fe^{II}-3Fe^{III}-N^{3-}]$, and $[4Fe^{II}-3Fe^{III}-C^{4-}]$ states (Table 1 - columns HC = OH). For $2Fe^{II}-5Fe^{III}$, the $X = C^{4-}$ model is more consistent with the experimental structures than $X = N^{3-}$ in nearly all tabulated dimensions, and the RMS deviations for the core distances slightly improve from 0.04 Å to 0.03 Å upon protonation. At the same time, the $[2Fe^{II}-5Fe^{III}-N^{3-}]$ state cannot be definitively eliminated based on the interatomic distances alone. Comparing the best structures obtained with protonated homocitrate ligand, the $[2Fe^{II}-5Fe^{III}-C^{4-}]$ model is somewhat contracted relative to the crystal structure, with an average deviation of -0.02 Å, while the $4Fe^{II}-3Fe^{III}$ oxidation state models are slightly expanded, with an average deviation of 0.02 Å; however, the overall RMS deviations are the same. To avoid overlooking compositions and oxidation states due to fortuitous error cancellation, we evaluated the possibility of $X = O^{2-}$ with the protonated model, but the RMS deviation for the core distances remains too high (0.09 Å), with considerable deviations in the $Fe^{(Fe)}-X$ (0.13 Å) and $Fe^{(Fe)}\cdots Fe^{(Mo)}$ (0.16 Å) distances. Also, the results for the $O_{hydroxyl}$-protonated $6Fe^{II}-1Fe^{III}-N^{3-}$ state (see Table S5) show unreasonable large geometric differences relative to the experimental structure.

3.5 Reduction Potentials

Reduction potentials were considered as energetic criteria for evaluating the oxidation state and composition of FeMo-co. The reduction potential of the FeMo-co^{Ox}/FeMo-co^{N} pair was calculated for the $2Fe^{II}-5Fe^{III}$, $4Fe^{II}-3Fe^{III}$ and $6Fe^{II}-1Fe^{III}$ states with C^{4-}, N^{3-}, or O^{2-}, covering a large range of charges (from -5 to -1 for our model), in addition to two of the $O_{hydroxyl}$-protonated models favored in the structural studies described above. For FeMo-co^{Ox}, we used the spin states shown in this work to be lowest in energy: $M_s = 0$ for $1Fe^{II}-6Fe^{III}$, and $M_s = 1$ for $3Fe^{II}-4Fe^{III}$ and $5Fe^{II}-2Fe^{III}$. The ligand protonation state is assumed to be unchanged during the reduction process, and this is supported by an EXAFS study showing a 0.03 Å increase in the average Mo-O/N distance upon reduction,[78] which is also reproduced in our calculations.

Table 3 summarizes the calculated reduction potentials along with a decomposition analysis according to Eqs. (1)-(3). The reduction potentials for the models with deprotonated

homocitrate range from -2.68 V to $+0.59$ V for the most and least negatively charged states, $[6Fe^{II}\text{-}1Fe^{III}\text{-}N^{3-}]^{5-}$ and $[2Fe^{II}\text{-}5Fe^{III}\text{-}N^{3-}]^{-}$, respectively, while the experimental value lies between these extremes at -0.042 V.[11] Examining the intermediately charged states, the $[4Fe^{II}\text{-}3Fe^{III}\text{-}N^{3-}]^{3-}$ is still too negatively charged ($E^{\circ\circ} = -0.83$ V), but $[2Fe^{II}\text{-}5Fe^{III}\text{-}C^{4-}]^{2-}$ gives $E^{\circ} = 0.00$ V, which is close to the experimental value. However, as discussed above, models with protonated $O_{hydroxyl}$ groups (denoted with +H) need to be considered. Thus, by evaluating protonated models we find that the reduction potentials for $[4Fe^{II}\text{-}3Fe^{III}\text{-}N^{3-}+H]^{2-}$ and $[2Fe^{II}\text{-}5Fe^{III}\text{-}C^{4-}+H]^{-}$ are -0.34 V and 0.38 V, respectively, nearly equidistant from the experimental value in opposite directions, and both can be considered as favored by this criterion.

Although reduction potentials alone do not rule out either of the $O_{hydroxyl}$-protonated models, they exhibit a general trend that allows for the elimination of models on the basis of overall cluster charge. For example, we can readily rule out the $[2Fe^{II}\text{-}5Fe^{III}\text{-}N^{3-}+H]$ state for FeMo-co^{N}, because its neutral total charge would render its reduction potential even more positive than that of $[2Fe^{II}\text{-}5Fe^{III}\text{-}N^{3-}]^{-}$ (0.59 V) and $[2Fe^{II}\text{-}5Fe^{III}\text{-}C^{4-}+H]^{-}$ (0.38 V). The calculated reduction potentials indicate the overall charge of the truncated FeMo-co^{N} model is likely -2 or -1. Considering the -3 charge of the full homocitrate ligand compared to -1 for the glycolate with protonated hydroxyl groups in both, we expect the overall charge of FeMo-co^{N} to be -4 or -3. Previous work indicated the charge of exFeMo-co^{Ox} is -2,[13] corresponding to a total charge of -3 for FeMo-co^{N} (-1 for our model). Thus, these charge considerations show a preference for the $2Fe^{II}\text{-}5Fe^{III}$ oxidation state distribution with $X = C^{4-}$ and protonated homocitrate.

By analyzing each component of the reduction potential calculations, we find that the major contributions are from the ionization potential ($\Delta\varepsilon_{SCF}$ or $\Delta\varepsilon_{SCF}^{s.p.}$) and the electronic solute-solvent interactions ($\Delta\Delta G_{elec}$). Corrections accounting for differences in protein-embedded structures upon reducing FeMo-co ($\Delta G^{\circ}_{solute\ corrections}$) improve the reduction potential by up to 150 mV,[79] while spin projection (s.p. – using two spin projection method) and non-electrostatic solute-solvent interactions ($\Delta\Delta G_{non}$) each account for less than 40 mV. While none of these corrections are negligible, the first approximation of using the SCF energies ($\Delta\varepsilon_{SCF} + \Delta\Delta G_{electrostatic}$) to calculate the reduction potential results in an error of only 10 mV for the $[2Fe^{II}\text{-}5Fe^{III}\text{-}C^{4-}+H]$ state and even less for the $[4Fe^{II}\text{-}3Fe^{III}\text{-}N^{3-}+H]$ state due to error cancellations. However, this cancellation is not universal, since we find a larger error in certain cases (e.g., 90 mV for the $[2Fe^{II}\text{-}5Fe^{III}\text{-}C^{4-}]$ model). Importantly, the overall conclusions derived from reduction potential calculations remain the same regardless of how the reduction potentials are calculated.

3.6 Spectroscopic Properties

In addition to composition, geometric structure, and relative energies of spin and oxidation states, we also examined the electronic structural information from Mössbauer and ENDOR spectroscopic measurements. These have been used in literature as dominant criteria to differentiate among various proposals for the structure and composition of FeMo-co, since they are highly sensitive to oxidation state, ligand environment, and geometric structure.[80] We find that the calculated Mössbauer isomer shifts, quadrupole splittings, and ENDOR hyperfine coupling constants are greatly affected by the composition of the experimental training set, and the employed level of theory.

3.6.1. Mössbauer Isomer Shifts—The currently accepted process of calculating Mössbauer isomer shifts requires the derivation of an empirical relationship between calculated electron density values at the nucleus ($\rho(0)$) and experimental isomer shifts for a set of model compounds at a given level of theory. For our training set we have employed a

variety of [Fe-S] and [Mo-Fe-S] clusters that are the closest models for the coordination environment of the Fe centers in FeMo-co. Since most of the published isomer shifts for the training set are for solid state samples (see Tables S6 and S7), it was most appropriate to use the crystallographic structures in the calculations (see Table S6 method 1), yielding a best fit to Eq. (9) of $\delta = -0.620\ e^{-1}\ a_0^3$ mm s^{-1} ($\rho(0) - 11833\ e\ a_0^{-3}$) + 0.563 mm s^{-1} (Figure S1A) with a standard deviation of 0.06 mm s^{-1}. From this equation, the isomer shifts were derived using the calculated average $\rho(0)$ of the Fe centers in FeMo-co in the structurally optimized $2Fe^{II}$-$5Fe^{III}$, $4Fe^{II}$-$3Fe^{III}$ and $6Fe^{II}$-$1Fe^{III}$ states with C^{4-} or N^{3-}.

As shown by the δ_1 values in Table 4 (see Table S8 for individual site δ values), isomer shift decreases by an average of 0.13 mm s^{-1} with oxidation along the series from $6Fe^{II}$-$1Fe^{III}$ to $4Fe^{II}$-$3Fe^{III}$ to $2Fe^{II}$-$5Fe^{III}$ with X = N^{3-}. Interestingly, the isomer shift decreases by about 0.05 mm s^{-1} in going from X = N^{3-} to C^{4-} due to an increase in $\rho(0)$, which is, in turn, likely caused by increased overlap with the Fe(4s) as discussed by Neese[81] for a series of Fe halides. The average isomer shift of the $[2Fe^{II}$-$5Fe^{III}$-$N^{3-}]$ state (0.41 mm s^{-1}) agrees best with the experimental[15] value of 0.41 mm s^{-1}, followed by the $[4Fe^{II}$-$3Fe^{III}$-C^{4-}+H] state (0.45 mm s^{-1}). Notably none of these states and compositions were shown above to be favored by other criteria. As with the reduction potentials, the average isomer shift of the most likely hydroxyl-protonated states, $[2Fe^{II}$-$5Fe^{III}$-C^{4-}+H] and $[4Fe^{II}$-$3Fe^{III}$-N^{3-}+H], lie nearly equidistant from the experimental value, at 0.32 mm s^{-1} and 0.51 mm s^{-1}, respectively.

Alternatively, the training set structures can be optimized in order to use the minimum energy structure for the employed computational method, as often preferred.[16, 63, 82] The best fit for the set of optimized structures (see Table S6 method 2) is $\delta = -0.744\ e^{-1}\ a_0^3$ mm s^{-1} ($\rho(0) - 11833\ e\ a_0^{-3}$) + 0.593 mm s^{-1} (Figure S1B), with a standard deviation of 0.04 mm s^{-1}. This fit appears to be significantly different than the previous fit; however, the effect on the calculated average isomer shift of FeMo-co is only 0.01 mm s^{-1} on average over the eight listed states. For consistency, the FeMo-co structure should also be optimized at the BP86/all-electron STO-TZP level as used for the training set. With the optimized structures, the average isomer shifts of the $[2Fe^{II}$-$5Fe^{III}$-C^{4-}+H] and $[4Fe^{II}$-$3Fe^{III}$-N^{3-}+H] states are 0.22 mm s^{-1} and 0.45 mm s^{-1}, respectively; thus, the latter state is favored with this method.

Importantly, a significant drawback of the isomer shift fitting procedure is the dependence on the choice of model compounds for the training set. The slopes of $\alpha = -0.620\ e^{-1}\ a_0^3$ mm s^{-1} or $-0.744\ e^{-1}\ a_0^3$ mm s^{-1} from method 1 and method 2 above, respectively, are steeper than the published values ranging between -0.3 and $-0.5\ e^{-1}\ a_0^3$ mm s^{-1}.[16, 18, 83] We note that the two models with the largest deviation from the correlation line in Figure S1A are $[Fe(S_2$-o-$Xyl)_2]^-$ and $[Fe_2S_2(S_2$-o-$Xyl)_2]^{2-}$, and their experimental isomer shifts of 0.13 mm s^{-1} and 0.17 mm s^{-1}, respectively,[84, 85] are much lower than values typically used for $[Fe^{III}$-S] complexes in training sets (for example Refs. 16, 17, 83). Rao and Holm used 0.28 mm s^{-1} as the lowest isomer shift for an $[Fe^{III}$-S] complex in their evaluation of the linear relationship between isomer shifts and oxidation state.[86] Notably, their fit predicts 0.40 mm s^{-1} for the $2Fe^{II}$-$5Fe^{III}$ oxidation state and 0.51 mm s^{-1} for $4Fe^{II}$-$3Fe^{III}$. Thus, if we remove these outliers (see Table S6 method 3), the new correlation line is described by $\delta = -0.491\ e^{-1}\ a_0^3$ mm s^{-1} ($\rho(0) - 11833\ e\ a_0^{-3}$) + 0.568 mm s^{-1} (Figure S1C), with a standard deviation of 0.04 mm s^{-1}, and the slope is more consistent with the aforementioned published values. With this method, the average isomer shifts of the $[2Fe^{II}$-$5Fe^{III}$-C^{4-}+H] and $[4Fe^{II}$-$3Fe^{III}$-N^{3-}+H] states become 0.38 mm s^{-1} and 0.52 mm s^{-1} (δ_3 values in Table 4), respectively, favoring the former.

The three described methods produce significantly different sets of data, resulting in a large error bar for the calculated isomer shifts. For example, the isomer shifts of the [$2Fe^{II}$-$5Fe^{III}$-C^{4-}+H] state were calculated within a range of 0.16 mm s^{-1}. The second method yields the smallest isomer shifts. In order to estimate the δ_2 values for other states not explicitly calculated, we can subtract 0.16 mm s^{-1} from the maximum calculated isomer shift for each state, producing an assumed lower limit for δ_2 (see Table 4), because the range used is much larger than that observed for [$4Fe^{II}$-$3Fe^{III}$-C^{4-}+H] (0.07 mm s^{-1}). Then, after taking into account the standard deviations of each method (e.g., δ_3 values carry an error bar of 0.04 mm s^{-1}), we find that all evaluated states except [$6Fe^{II}$-$1Fe^{III}$-N^{3-}] have theoretical isomer shifts around the experimental value. We can consider the third method to be the most appropriate due to the exclusion of training set complexes with unusually low isomer shifts. Furthermore, the third method uses structures optimized with our standard, previously validated procedure, and is thus expected to be more accurate than the second method. Thus, the δ_3 values can be considered as a stringent criterion for selecting only the $2Fe^{II}$-$5Fe^{III}$ oxidation state with C^{4-} or N^{3-} central ligands as preferred assignments, with or without protonated homocitrate ligand.

3.6.2 Mössbauer Quadrupole Splitting—First, we carried out of an evaluation of the calculated Mössbauer quadrupole splitting parameters (ΔE_Q) using the same training set as for the isomer shift calculations (see above). The absolute values of ΔE_Q for the selected Fe sites are found to have an RMS deviation of 0.31 mm s^{-1} from the experiment when using crystallographic coordinates, and 0.32 mm s^{-1} for the corresponding optimized structures (see Table S6), which is a typical level of accuracy.[63, 80, 83] The calculated ΔE_Q values for the $2Fe^{II}$-$5Fe^{III}$, $4Fe^{II}$-$3Fe^{III}$ and $6Fe^{II}$-$1Fe^{III}$ states with C^{4-} or N^{3-} are presented in Table 4 (see Table S9 for individual site ΔE_Q values). The sign of ΔE_Q is difficult to calculate reliably,[87] and thus not surprisingly, none of the oxidation states or compositions match the experimental distribution of six negative and one positive ΔE_Q in our calculations. To facilitate comparison of the theoretical and experimental quadrupole splitting values, we take the mean of $|\Delta E_Q|$ over the Fe sites and find a range of 0.86 mm s^{-1} ([$2Fe^{II}$-$5Fe^{III}$-C^{4-}] +H) to 1.13 mm s^{-1} ([$2Fe^{II}$-$5Fe^{III}$-N^{3-}]) for the various states. These are all overestimated relative to the experimental value of 0.69 mm s^{-1}, although considering the error bar of 0.32 mm s^{-1}, all tested states except the deprotonated [$2Fe^{II}$-$5Fe^{III}$-N^{3-}] and [$4Fe^{II}$-$3Fe^{III}$-N^{3-}] give results consistent with experiment, indicating the difficulty of distinguishing between states by this criterion.

The lowest four calculated mean $|\Delta E_Q|$ values are attributed to states with X = C^{4-} and the highest four to those with X = N^{3-}, while there is no obvious correlation with oxidation state. However, there is a strong correspondence between the ordering of states by increasing mean absolute Fe spin density ($|\rho_s(Fe)|$) and increasing $|\Delta E_Q|$ with only one exception ($2Fe^{II}$-$5Fe^{III}$-N^{3-}, see Table S10 for individual site $\rho_s(Fe)$ values). This correlation indicates that the dominant factors affecting spin densities including bond covalency and the employed level of theory also strongly influence ΔE_Q values. Indeed, a change in functional that increases Fe spin density also increases the $|\Delta E_Q|$ values for the two most favored states from the compositional, structural and energetic considerations, [$2Fe^{II}$-$5Fe^{III}$-C^{4-}+H] and [$4Fe^{II}$-$3Fe^{III}$-N^{3-}+H], from 0.86 mm s^{-1} and 0.97 mm s^{-1} (BP86) to 1.16 mm s^{-1} and 1.43 mm s^{-1} (B3LYP). The [$2Fe^{II}$-$5Fe^{III}$-C^{4-}+H] state is consistently the closest to the experiment, but the accuracy of these calculations, as demonstrated with the training set, is not high enough to give strong preference to this state.

3.6.3 Hyperfine Couplings—Due to the limitations for describing accurate hyperfine couplings of transition metal nuclei from *ab initio* calculations, the ^{57}Fe hyperfine coupling constants (a_i^{calc}) were determined through a semi-empirical procedure (see Methods Section) as previously applied by Noodleman *et al.* [25] for the [$4Fe^{II}$-$3Fe^{III}$-N^{3-}] state. We

extended these calculations to the $2Fe^{II}$-$5Fe^{III}$, $4Fe^{II}$-$3Fe^{III}$ and $6Fe^{II}$-$1Fe^{III}$ states with C^{4-}, N^{3-}, or O^{2-}. The resulting a_i^{calc} values (see Table S11) are summed over the seven Fe sites to give a^{test}, a straightforward parameter introduced by Mouesca et al.[68] for comparison with experimental data. The results in Table 4 show that the a^{test} value of the [$2Fe^{II}$-$5Fe^{III}$-C^{4-}+H] state (−23.8 MHz) is closest to that of the Mössbauer experiment (−17.9 MHz),[15] while the [$4Fe^{II}$-$3Fe^{III}$-O^{2-}] (−29.5 MHz) and [$6Fe^{II}$-$1Fe^{III}$-N^{3-}] (−29.6 MHz) states have the largest deviations. Although the spin projection coefficients, K_i, are dependent on the oxidation state assignments of each iron site (see Table S12), spin densities are the dominant factors contributing to differences in a^{test} in this series. As with the quadrupole splittings, there is a nearly perfect correspondence between the ordering of FeMo-co states arranged by a^{test} values from least to most negative, and the ordering by increasing $|\rho_s(Fe)|$, with the only exception being the [$6Fe^{II}$-$1Fe^{III}$-N^{3-}] state, which has an intermediate $|\rho_s(Fe)|$. Due to the reliance on atomic spin density values, the a^{test} values are highly dependent on the employed functional and basis set. In addition to the BP86/SDD-VTZ(d) level of theory used for the series, the [$2Fe^{II}$-$5Fe^{III}$-C^{4-}+H] and [$4Fe^{II}$-$3Fe^{III}$-N^{3-}+H] states were evaluated with B3LYP/SDD-VTZ(d) and B(5HF)P86/6-311+G(d), which has been found previously[39] to be excellent for [Fe-S] cluster spin densities. With B3LYP/SDD-VTZ(d), a^{test} becomes more negative for both states and the difference between them increases from −3.1 MHz to −6.4 MHz, while with B(5HF)P86/6-311+G(d), the gap decreases to −0.9 MHz. Despite strong computational method dependence, the [$2Fe^{II}$-$5Fe^{III}$-C^{4-}+H] state consistently has the closest a^{test} to experiment.

As a further analysis of the hyperfine couplings, and to avoid possible error cancellation caused by the summation of positive and negative values in determining a^{test}, the RMS deviation of the individual site a_i^{calc} values were also compared (Table 4). Since the specific Fe site corresponding to an experimental a_i is unknown, the RMS deviations were calculated by ordering the a_i values numerically. Here, again, the [$2Fe^{II}$-$5Fe^{III}$-C^{4-}+H] state has the smallest RMS deviation of 3.3 MHz, compared to 5.5 MHz for [$4Fe^{II}$-$3Fe^{III}$-C^{4-}+H], and the largest value of 6.8 MHz for [$4Fe^{II}$-$3Fe^{III}$-O^{2-}]. The ordering of states is generally the same as for a^{test} with some minor rearrangements. With B3LYP the RMS deviations increase by about 2.5 MHz, while with B(5HF)P86/6-311+G(d) the results improve, yielding 2.7 MHz for [$2Fe^{II}$-$5Fe^{III}$-C^{4-}+H]. Overall, the hyperfine coupling calculations favor both protonation states of [$2Fe^{II}$-$5Fe^{III}$-C^{4-}]. Since the error is difficult to estimate, other states cannot be excluded based on this criteria alone.

Advanced EPR methods, such as ENDOR and ESEEM techniques, are ideal for detecting weakly coupled spin systems, such as an interstitial atom within the central 6Fe belt in the BS7 state (see Section 3.1 for description). On the basis of the lack of a central ^{13}C, or $^{14/15}N$ atom signal it was suggested that if the interstitial ligand X is C^{4-} or N^{3-} then the $a_{iso}(^{13}C)$ or $a_{iso}(^{14}N)$ coupling constants must be less than 0.05-0.1 MHz or 0.03-0.07 MHz, respectively.[25] Table 4 shows the calculated $a_{iso}(X)$ values for the same series of FeMo-co states used for the Mössbauer parameters. In each state $a_{iso}(X)$ is higher than the experimental detection limit with the lowest absolute value of 0.3 MHz for the [$4Fe^{II}$-$3Fe^{III}$-N^{3-}] and [$6Fe^{II}$-$1Fe^{III}$-N^{3-}] states. The dependence on the computational method is strong, since switching from BP86 to B3LYP functional approximately doubles $a_{iso}(X)$. Thus, we conclude that the required level of accuracy to reproduce a very small hyperfine coupling for X is out of reach with current DFT functionals, even when employing a level of theory calibrated to experimental metal-ligand bonding information.

4. Conclusions

In this work, we applied broken symmetry DFT calculations with spectroscopically (XAS) calibrated functionals and saturated basis sets to provide a comprehensive evaluation of the

available experimental information about the electronic, geometric, energetic, and magnetic properties of the protein-bound nitrogenase FeMo-co. We found that the relative energies of spin coupling schemes are dominantly governed by the number of antiferromagnetic interactions, including those mediated by the interstitial ligand (X). The ground state spin coupling scheme, BS7, has the maximum number of antiferromagnetic M-S/X-M interactions. Using the BS7 spin coupling scheme, we calculated the ground spin state for oxidized and resting FeMo-co, geometric structures, reduction potentials, and Mössbauer and hyperfine parameters for the oxidation states $6Fe^{II}$-$1Fe^{III}$, $4Fe^{II}$-$3Fe^{III}$, and $2Fe^{II}$-$5Fe^{III}$ assuming the presence of weak-field ligand environment at the Fe centers with 10-electron interstitial ligands C^{4-}, N^{3-}, and O^{2-}.

Table 5 summarizes the preferred oxidation states for the iron centers and compositions for the interstitial atom based on independent experimental criteria and homocitrate protonation states. The findings for each criterion follow:

(1) We are not able to rule out any possibilities based on the ground spin state of resting FeMo-co, as each is consistent with the experimental $S_t = 3/2$ state.

(2) However, only the $2Fe^{II}$-$5Fe^{III}$ oxidation state is consistent with the $S_t = 0$ ground oxidized form.

(3) The optimized geometries with deprotonated homocitrate favor the $2Fe^{II}$-$5Fe^{III}$ states with C^{4-} or N^{3-}, while strongly disfavoring O^{2-} and protonated forms of the central ions due to an unreasonable expansion of the central '6Fe-belt' relative to the crystal structure. Contrary to what is expected based on size, a highly charged, larger interstitial atom with lower electronegativity is preferred over a smaller, more electronegative ion to maintain the cluster core geometry. The optimized FeMo-co^N structures consistently show that the Mo-$O_{hydroxyl}$ bond length is far too short (0.14 to 0.21 Å) relative to its experimental value for all oxidation states and compositions. This discrepancy was eliminated by protonating the coordinated $O_{hydroxyl}$ group. With the $O_{hydroxyl}$-protonated model, the $[2Fe^{II}$-$5Fe^{III}$-$C^{4-}+H]$, $[4Fe^{II}$-$3Fe^{III}$-$C^{4-}+H]$ and $[4Fe^{II}$-$3Fe^{III}$-$N^{3-}+H]$ states show the closest agreement with the experimental structures.

(4) The $[2Fe^{II}$-$5Fe^{III}$-$C^{4-}+H]$ state is preferred based on the experimentally consistent −2 charge in the FeMo-co^{Ox} or exFeMo-co^{Ox} form.

(5) The states with the most reasonable reduction potentials for FeMo-co^{Ox}/FeMo-co^N all carry a total charge of −1 or −2. It is important to emphasize that a solely reduction potential-based evaluation of composition can be misleading, since the reduction potential for the $[4Fe^{II}$-$3Fe^{III}$-$O^{2-}]$ state with −2 total charge only deviates 10 mV from experiment, despite significant disagreement in other criteria. Alternative models such as $[4Fe^{II}$-$3Fe^{III}$-$N^{3-}+H]$ with a protonated bridging sulfide ligand are also expected to have favorable reduction potentials based on the overall charge despite the already reported[18] cluster expansion. The reduction potentials of $[2Fe^{II}$-$5Fe^{III}$-$C^{4-}+H]$ (0.38 V) and $[4Fe^{II}$-$3Fe^{III}$-$N^{3-}+H]$ (−0.34 V) are the closest to the experimental value of −0.042 V.

(6) Mössbauer isomer shift calculations are strongly dependent on the employed training set composition and structural optimization state, but with our favored method only the $2Fe^{II}$-$5Fe^{III}$ states with C^{4-} or N^{3-} yield experimentally consistent values.

(7) The quadrupole splittings are closest to experiment with $[2Fe^{II}$-$5Fe^{III}$-$C^{4-}+H]$, but the large error bars overlap the experimental value for nearly all tested states.

(8) Current DFT methods does not have the required accuracy for calculating unambiguously hyperfine couplings in a multinuclear, delocalized mixed-valence, spin-coupled system, such as FeMo-co. Nevertheless, the $2Fe^{II}$-$5Fe^{III}$ oxidation state with C^{4-} has ^{57}Fe hyperfine couplings is the least inconsistent with experiment with respect to both a^{test} and RMS deviation of the individual site parameters, a_i.

(9) The hyperfine coupling for the central ligand X is larger than the limits set by experiment, regardless of composition and oxidation state, likely due to the aforementioned limited accuracy.

In conclusion, only $[2Fe^{II}$-$5Fe^{III}$-C^{4-}+H]$ is consistently favored, and we consider it to be the most likely oxidation state and composition. The $[4Fe^{II}$-$3Fe^{III}$-N^{3-}+H]$ state is the second best, as it passed the structural (with only the protonated homocitrate) and reduction potential criteria; however, it failed with respect to the relative energies of oxidized spin states, the overall charge, the isomer shifts and the hyperfine parameters. The more oxidized electronic state, the protonation state of the homocitrate, and the presence of a carbide central ligand open up exciting further directions in investigating the molecular mechanism of biological nitrogen fixation and the biosynthesis of the FeMo-cofactor of nitrogenase.

Supplementary Material

Refer to Web version on PubMed Central for supplementary material.

Acknowledgments

References

1. Peters JW, Szilagyi RK. Exploring new frontiers of nitrogenase structure and mechanism. Curr. Opin. Chem. Biol. 2006; 10:101–108. [PubMed: 16510305]

2. Einsle O, Tezcan FA, Andrade SLA, Schmid B, Yoshida M, Howard JB, Rees DC. Nitrogenase MoFe-protein at 1.16 Å resolution: a central ligand in the FeMo-cofactor. Science. 2002; 297:1696–1700. [PubMed: 12215645]

3. Igarashi RY, Seefeldt LC. Nitrogen fixation: the mechanism of the Mo-dependent nitrogenase. Crit. Rev. Biochem. Mol. Biol. 2003; 38:351–384. [PubMed: 14551236]

4. Venters RA, Nelson MJ, McLean PA, True AE, Levy MA, Hoffman BM, Orme-Johnson WH. ENDOR of the Resting State of Nitrogenase Molybdenum Iron Proteins from *Azotobacter vinelandii, Klebsiella pneumoniae*, and *Clostridium pasteurianum*: ^{1}H, ^{57}Fe, ^{95}Mo, and ^{33}S Studies. J. Am. Chem. Soc. 1986; 108:3487–3498.

5. Hedman B, Frank P, Gheller SF, Roe AL, Newton WE, Hodgson KO. New structural insights into the iron-molybdenum cofactor from *Azotobacter vinelandii* nitrogenase through sulfur K and molybdenum L X-ray absorption edge studies. J. Am. Chem. Soc. 1988; 110:3798–3805.

6. Corbett MC, Tezcan FA, Einsle O, Walton MY, Rees DC, Latimer MJ, Hedman B, Hodgson KO. Mo K- and L-edge X-ray absorption spectroscopic study of the ADP·AlF$_4^-$-stabilized nitrogenase complex: comparison with MoFe protein in solution and single crystal. J. Synchrotron Rad. 2005; 12:28–34.

7. Huynh BH, Münck E, Orme-Johnson WH. Nitrogenase XI: Mössbauer studies on the cofactor centers of the MoFe protein from *Azotobacter vinelandii* OP. Biochim. Biophys. Acta. 1979; 576:192–203. [PubMed: 760805]

8. Huynh BH, Henzl MT, Christner JA, Zimmermann R, Orme-Johnson WH, Münck E. Nitrogenase XII: Mössbauer studies of the MoFe protein from *Clostridum pasteurianum* W5. Biochim. Biophys. Acta. 1980; 623:124–138. [PubMed: 6246963]

9. Johnson MK, Thomson AJ, Robinson AE, Smith BE. Characterization of the paramagnetic centers of the molybdenum-iron protein of nitrogenase from *Klebsiella pneumoniae* using low temperature magnetic circular dichroism spectroscopy. Biochim. Biophys. Acta. 1981; 671:61–70.

10. Conradson SD, Burgess BK, Holm RH. Fluorine-19 chemical shifts as probes of the structure and reactivity of the iron-molybdenum cofactor of nitrogenase. J. Biol. Chem. 1988; 263:13743–13749. [PubMed: 2843534]

11. O'Donnell MJ, Smith BE. Electron-Paramagnetic-Resonance Studies on Redox Properties of Molybdenum-Iron Protein of Nitrogenase between +50 and −450 Mv. Biochem. J. 1978; 173:831–839. [PubMed: 30448]

12. Pickett CJ, Vincent KA, Ibrahim SK, Gormal CA, Smith BE, Best SP. Electron-transfer chemistry of the iron-molybdenum cofactor of nitrogenase: delocalized and localized reduced states of FeMoco which allow binding of carbon monoxide to iron and molybdenum. Chem. Eur. J. 2003; 9:76–87.

13. Huang HQ, Kofford M, Simpson FB, Watt GD. Purification, composition, charge, and molecular weight of the FeMo cofactor from *Azotobacter vinelandii* nitrogenase. J. Inorg. Biochem. 1993; 52:59–75. [PubMed: 8228979]

14. Lee HI, Hales BJ, Hoffman BM. Metal-ion valencies of the FeMo cofactor in CO-inhibited and resting state nitrogenase by ^{57}Fe Q-band ENDOR. J. Am. Chem. Soc. 1997; 119:11395–11400.

15. Yoo SJ, Angove HC, Papaefthymiou V, Burgess BK, Münck E. Mössbauer study of the MoFe protein of nitrogenase from *Azotobacter vinelandii* using selective ^{57}Fe enrichment of the M-centers. J. Am. Chem. Soc. 2000; 122:4926–4936.

16. Vrajmasu V, Münck E, Bominaar EL. Density functional study of the electric hyperfine interactions and the redox-structural correlations in the cofactor of nitrogenase. Analysis of general trends in ^{57}Fe isomer shifts. Inorg. Chem. 2003; 42:5974–5988. [PubMed: 12971768]

17. Lovell T, Li J, Liu TQ, Case DA, Noodleman L. FeMo cofactor of nitrogenase: a density functional study of states M^N, M^{OX}, M^R, and M^I. J. Am. Chem. Soc. 2001; 123:12392–12410. [PubMed: 11734043]

18. Lovell T, Liu TQ, Case DA, Noodleman L. Structural, spectroscopic, and redox consequences of central ligand in the FeMoco of nitrogenase: a density functional theoretical study. J. Am. Chem. Soc. 2003; 125:8377–8383. [PubMed: 12837110]

19. Dance I. The consequences of an interstitial N atom in the FeMo cofactor of nitrogenase. Chem. Commun. 2003:324–325.

20. Dance I. The correlation of redox potential, HOMO energy, and oxidation state in metal sulfide clusters and its application to determine the redox level of the FeMo-co active-site cluster of nitrogenase. Inorg. Chem. 2006; 45:5084–5091. [PubMed: 16780330]

21. Schimpl J, Petrilli HM, Blöchl PE. Nitrogen binding to the FeMo-cofactor of nitrogenase. J. Am. Chem. Soc. 2003; 125:15772–15778. [PubMed: 14677967]

22. True AE, Nelson MJ, Venters RA, Orme-Johnson WH, Hoffman BM. ^{57}Fe hyperfine coupling tensors of the FeMo cluster in *Azotobacter vinelandii* MoFe Protein: determination by polycrystalline ENDOR spectroscopy. J. Am. Chem. Soc. 1988; 110:1935–1943.

23. Neese F. Prediction of molecular properties and molecular spectroscopy with density functional theory: from fundamental theory to exchange-coupling. Coord. Chem. Rev. 2009; 253:526–563.

24. Noodleman L. Valence bond description of anti-ferromagnetic coupling in transition-metal dimers. J. Chem. Phys. 1981; 74:5737–5743.

25. Lukoyanov D, Pelmenschikov V, Maeser N, Laryukhin M, Yang TC, Noodleman L, Dean DR, Case DA, Seefeldt LC, Hoffman BM. Testing if the interstitial atom, X, of the nitrogenase molybdenum-iron cofactor is N or C: ENDOR, ESEEM, and DFT studies of the $S = 3/2$ resting state in multiple environments. Inorg. Chem. 2007; 46:11437–11449. [PubMed: 18027933]

26. Pickett CJ. The Chatt cycle and the mechanism of enzymic reduction of molecular nitrogen. J. Biol. Inorg. Chem. 1996; 1:601–606.

27. Kästner J, Blöchl PE. Ammonia production at the FeMo cofactor of nitrogenase: results from density functional theory. J. Am. Chem. Soc. 2007; 129:2998–3006. [PubMed: 17309262]

28. Huniar U, Ahlrichs R, Coucouvanis D. Density functional theory calculations and exploration of a possible mechanism of N_2 reduction by nitrogenase. J. Am. Chem. Soc. 2004; 126:2588–2601. [PubMed: 14982469]

29. Szilagyi RK, Musaev DG, Morokuma K. Theoretical studies of biological nitrogen fixation. Part II. Hydrogen bonded networks as possible reactant and product channels. J. Mol. Struct. Theochem. 2000; 506:131–146.

30. Durrant MC, Francis A, Lowe DJ, Newton WE, Fisher K. Evidence for a dynamic role for homocitrate during nitrogen fixation: the effect of substitution at the α-Lys[426] position in MoFe-protein of *Azotobacter vinelandii*. Biochem. J. 2006; 397:261–270. [PubMed: 16566750]

31. Frisch, MJ., et al. Gaussian 03. Rev E.01. Gaussian, Inc; Wallingford, CT: 2006.

32. Becke AD. Density-functional exchange-energy approximation with correct asymptotic behavior. Phys. Rev. A. 1988; 38:3098–3100. [PubMed: 9900728]

33. Perdew JP. Density-functional approximation for the correlation energy of the inhomogeneous electron gas. Phys. Rev. B. 1986; 33:8822–8824.

34. Dunning, TH., Jr.; Hay, PJ. Modern Theoretical Chemistry. Schaefer, HF., III, editor. Vol. Vol. 3. Plenum; New York: 1976. p. 1-28.

35. Dolg M, Wedig U, Stoll H, Preuss H. Energy-adjusted *ab initio* pseudopotentials for the first row transition elements. J. Chem. Phys. 1987; 86:866–872.

36. Wedig, U.; Dolg, M.; Stoll, H.; Preuss, H. Quantum Chemistry: The Challenge of Transition Metals and Coordination Chemistry. Veillard, A., editor. Reidel; Dordrecht, The Netherlands: 1986. p. 79

37. Ehlers AW, Bohme M, Dapprich S, Gobbi A, Hollwarth A, Jonas V, Kohler KF, Stegmann R, Veldkamp A, Frenking G. A set of f-polarization functions for pseudo-potential basis sets of the transition metals Sc-Cu, Y-Ag and La-Au. Chem. Phys. Lett. 1993; 208:111–114.

38. Hollwarth A, Bohme M, Dapprich S, Ehlers AW, Gobbi A, Jonas V, Kohler KF, Stegmann R, Veldkamp A, Frenking G. A set of d-polarization functions for pseudo-potential basis sets of the main group elements Al-Bi and f-type polarization functions for Zn, Cd, Hg. Chem. Phys. Lett. 1993; 208:237–240.

39. Szilagyi RK, Winslow MA. On the accuracy of density functional theory for iron-sulfur clusters. J. Comput. Chem. 2006; 27:1385–1397. [PubMed: 16788911]

40. Becke AD. Density-functional thermochemistry. III. The role of exact exchange. J. Chem. Phys. 1993; 98:5648–5652.

41. Stephens PJ, Devlin FJ, Chabalowski CF, Frisch MJ. *Ab initio* calculation of vibrational absorption and circular dichroism spectra using density functional force fields. J. Phys. Chem. 1994; 98:11623–11627.

42. Curtiss LA, McGrath MP, Blaudeau JP, Davis NE, Binning RC, Radom L. Extension of Gaussian-2 Theory to Molecules Containing 3rd-Row Atoms Ga-Kr. J. Chem. Phys. 1995; 103:6104–6113.

43. Velde GT, Bickelhaupt FM, Baerends EJ, Guerra CF, Van Gisbergen SJA, Snijders JG, Ziegler T. Chemistry with ADF. J. Comput. Chem. 2001; 22:931–967.

44. Guerra CF, Snijders JG, te Velde G, Baerends EJ. Towards an order-N DFT method. Theor. Chem. Acc. 1998; 99:391–403.

45. ADF2009.01, SCM, Theoretical Chemistry. Vrije Universiteit; Amsterdam, The Netherlands: http://www.scm.com

46. Klamt A, Schuurmann G. Cosmo - a New Approach to Dielectric Screening in Solvents with Explicit Expressions for the Screening Energy and Its Gradient. J. Chem. Soc., Perkin Trans. 2. 1993:799–805.

47. Pye CC, Ziegler T. An implementation of the conductor-like screening model of solvation within the Amsterdam density functional package. Theor. Chem. Acc. 1999; 101:396–408.

48. Klamt A, Jonas V. Treatment of the outlying charge in continuum solvation models. J. Chem. Phys. 1996; 105:9972–9981.

49. Klamt A. Conductor-Like Screening Model for Real Solvents - a New Approach to the Quantitative Calculation of Solvation Phenomena. J. Phys. Chem. 1995; 99:2224–2235.

50. Tomasi J, Persico M. Molecular interactions in solution: an overview of methods based on continuous distributions of the solvent. Chem. Rev. 1994; 94:2027–2094.

51. Cossi M, Barone V, Cammi R, Tomasi J. *Ab initio* study of solvated molecules: a new implementation of the polarizable continuum model. Chem. Phys. Lett. 1996; 255:327–335.

52. Barone V, Cossi M, Tomasi J. Geometry optimization of molecular structures in solution by the polarizable continuum model. J. Comput. Chem. 1998; 19:404–417.

53. In the BS method, paramagnetic centers have majority spin-up or minority spin-down electrons, and the total system has a well-defined total spin quantum number (M_s). Although BS states are not pure spin states and do not represent a conceptually correct solution of the spin operator, their single-reference representation can be conveniently accessed by the DFT formalism and can accurately predict the geometric and electronic structural features of Fe-S clusters.

54. Clark AE, Davidson ER. Local spin. J. Chem. Phys. 2001; 115:7382–7392.

55. Shoji M, Koizumi K, Kitagawa Y, Kawakami T, Yamanaka S, Okumura M, Yamaguchi K. A general algorithm for calculation of Heisenberg exchange integrals *J* in multispin systems. Chem. Phys. Lett. 2006; 432:343–347.

56. Anderson PW, Hasegawa H. Considerations on Double Exchange. Physical Review. 1955; 100:675–681.

57. Orio M, Mouesca JM. Variation of average g values and effective exchange coupling constants among [2Fe-2S] clusters: A density functional theory study of the impact of localization (trapping forces) versus delocalization (double-exchange) as competing factors. Inorg. Chem. 2008; 47:5394–5416. [PubMed: 18491857]

58. Clemente-Juan JM, Borrás-Almenar JJ, Coronado E, Palii AV, Tsukerblat BS. High-Nuclearity Mixed-Valence Clusters and Mixed-Valence Chains: General Approach to the Calculation of the Energy Levels and Bulk Magnetic Properties. Inorg. Chem. 2009; 48:4557–4568. [PubMed: 19371089]

59. Dey A, Glaser T, Couture MMJ, Eltis LD, Holm RH, Hedman B, Hodgson KO, Solomon EI. Ligand K-Edge X-ray absorption spectroscopy of [Fe$_4$S$_4$]$^{1+,2+,3+}$ clusters: changes in bonding and electronic relaxation upon redox. J. Am. Chem. Soc. 2004; 126:8320–8328. [PubMed: 15225075]

60. Reed AE, Weinhold F. Natural bond orbital analysis of near-Hartree-Fock water dimer. J. Chem. Phys. 1983; 78:4066–4073.

61. The effect of second derivatives of the non-electrostatic interactions on $\Delta G°_{solute}$ were not included, but we expect this contribution to be negligible due to small structural changes upon redox chemistry in Fe-S clusters. The $\Delta G°_{solute}$ and $\Delta\Delta G°_{solvation}$ terms were calculated for BS states without spin projection correction to solvation terms.

62. Gas phase optimizations were only performed for one representative model, [4Fe^{II}-3Fe^{III}-N$^{3−}$] with protonated O$_{hydroxyl}$ of homocitrate.

63. Sinnecker S, Slep LD, Bill E, Neese F. Performance of nonrelativistic and quasi-relativistic hybrid DFT for the prediction of electric and magnetic hyperfine parameters in ^{57}Fe Mössbauer spectra. Inorg. Chem. 2005; 44:2245–2254. [PubMed: 15792459]

64. Munzarova M, Kaupp M. A critical validation of density functional and coupled-cluster approaches for the calculation of EPR hyperfine coupling constants in transition metal complexes. J. Phys. Chem. A. 1999; 103:9966–9983.

65. Pantazis DA, Orio M, Petrenko T, Zein S, Bill E, Lubitz W, Messinger J, Neese F. A New Quantum Chemical Approach to the Magnetic Properties of Oligonuclear Transition-Metal Complexes: Application to a Model for the Tetranuclear Manganese Cluster of Photosystem II. Chem. Eur. J. 2009; 15:5108–5123.

66. Greco C, Silakov A, Bruschi M, Ryde U, De Gioia L, Lubitz W. Magnetic Properties of [FeFe]-Hydrogenases: A Theoretical Investigation Based on Extended QM and QM/MM Models of the H-Cluster and Its Surroundings. Eur. J. Inorg. Chem. 2011:1043–1049.

67. Mouesca JM, Noodleman L, Case DA. Analysis of the ^{57}Fe hyperfine coupling constants and spin states in nitrogenase P-clusters. Inorg. Chem. 1994; 33:4819–4830.

68. Mouesca JM, Noodleman L, Case DA, Lamotte B. Spin densities and spin coupling in iron-sulfur clusters: a new analysis of hyperfine coupling constants. Inorg. Chem. 1995; 34:4347–4359.

69. Zhang Y, Mao JH, Oldfield E. [57]Fe Mössbauer isomer shifts of heme protein model systems: electronic structure calculations. J. Am. Chem. Soc. 2002; 124:7829–7839. [PubMed: 12083937]

70. Calculations involving other oxidation state distributions or compositions revealed that trends in the relative energies of spin coupling schemes are independent of the cluster composition and charge state.

71. Harris, TV.; Gardenghi, DJ.; Szilagyi, RK. Manuscript in preparation

72. Strange RW, Eady RR, Lawson D, Hasnain SS. XAFS studies of nitrogenase: the MoFe and VFe proteins and the use of crystallographic coordinates in three-dimensional EXAFS data analysis. J. Synchrotron Rad. 2003; 10:71–75.

73. To test the relationship between covalency, electronegativity and Fe-X bond length, we optimized the $4Fe^{II}$-$3Fe^{III}$ state with $X = F^-$, and the low covalency and high electronegativity led to bonds overly expanded by more than 0.40 Å, indicating the lack of ability to share sufficient electron density for covalent Fe-X bonds.

74. Hinnemann B, Nørskov JK. Modeling a central ligand in the nitrogenase FeMo cofactor. J. Am. Chem. Soc. 2003; 125:1466–1467. [PubMed: 12568592]

75. Gronberg KLC, Gormal CA, Durrant MC, Smith BE, Henderson RA. Why R-Homocitrate is essential to the reactivity of FeMo-cofactor of nitrogenase: Studies on NifV(−)-extracted FeMo-cofactor. J. Am. Chem. Soc. 1998; 120:10613–10621.

76. Durrant MC. Controlled protonation of iron-molybdenum cofactor by nitrogenase: a structural and theoretical analysis. Biochem. J. 2001; 355:569–576. [PubMed: 11311117]

77. Barney BM, Yurth MG, Dos Santos PC, Dean DR, Seefeldt LC. A substrate channel in the nitrogenase MoFe protein. J. Biol. Inorg. Chem. 2009; 14:1015–1022. [PubMed: 19458968]

78. Christiansen J, Tittsworth RC, Hales BJ, Cramer SP. Fe and Mo EXAFS of *Azotobacter Vinelandii* Nitrogenase in Partially Oxidized and Singly Reduced Forms. J. Am. Chem. Soc. 1995; 117:10017–10024.

79. The corrections accounting for changes in gas phase structure upon reducing FeMo-co, and those accounting for structural relaxation due to embedment in the PCM model partially cancel, leaving only one term, ΔG°_{solute}.

80. Zhang Y, Oldfield E. An investigation of the unusual [57]Fe Mössbauer quadrupole splittings and isomer shifts in 2 and 3-coordinate Fe(II) complexes. J. Phys. Chem. B. 2003; 107:7180–7188.

81. Neese F. Prediction and interpretation of the [57]Fe isomer shift in Mössbauer spectra by density functional theory. Inorg. Chim. Acta. 2002; 337:181–192.

82. Han WG, Liu TQ, Lovell T, Noodleman L. DFT calculations of [57]Fe Mössbauer isomer shifts and quadrupole splittings for iron complexes in polar dielectric media: applications to methane monooxygenase and ribonucleotide reductase. J. Comput. Chem. 2006; 27:1292–1306. [PubMed: 16786546]

83. Hopmann KH, Ghosh A, Noodleman L. Density functional theory calculations on Mössbauer parameters of nonheme iron nitrosyls. Inorg. Chem. 2009; 48:9155–9165. [PubMed: 19780615]

84. Lane RW, Ibers JA, Frankel RB, Holm RH. Synthetic analogs of active sites of iron-sulfur proteins: bis(*o*-xylyldithiolato)ferrate(III) monoanion, a structurally unconstrained model for rubredoxin Fe-S_4 unit. Proc. Natl. Acad. Sci. U. S. A. 1975; 72:2868–2872. [PubMed: 1059080]

85. Gillum WO, Frankel RB, Foner S, Holm RH. Synthetic analogs of active sites of iron-sulfur proteins. XIII. Further electronic structural relationships between analogs $[Fe_2S_2(SR)_4]^{2-}$ and active sites of oxidized 2Fe-2S proteins. Inorg. Chem. 1976; 15:1095–1100.

86. Rao PV, Holm RH. Synthetic analogues of the active sites of iron-sulfur proteins. Chem. Rev. 2004; 104:527–559. [PubMed: 14871134]

87. Han WG, Noodleman L. Quantum cluster size and solvent polarity effects on the geometries and Mössbauer properties of the active site model for ribonucleotide reductase intermediate X: a density functional theory study. Theor. Chem. Acc. 125:305–317. [PubMed: 20445806]
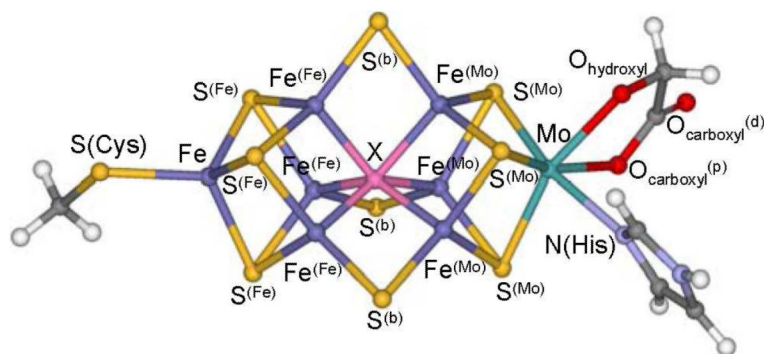
Figure 1.

Computational model of FeMo-co based on the 1.16 Å crystal structure of the MoFe protein from *Azotobacter vinelandii* (PDB ID 1M1N)[2].
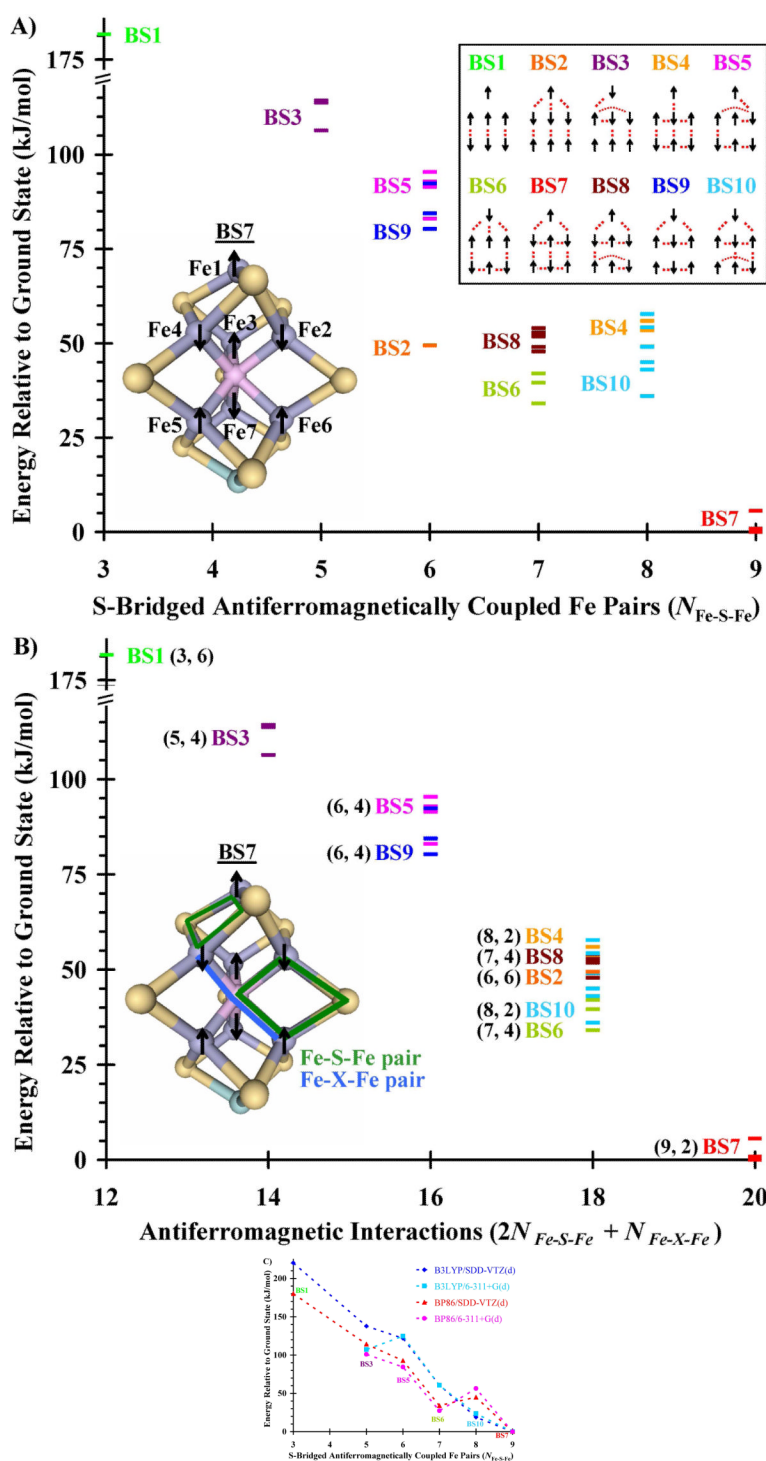
Figure 2.
Relative energies of the 35 individual spin states to the lowest energy state, BS7, plotted against (A) the number of sulfide bridged antiferromagnetically coupled Fe pairs and (B) the total number of antiferromagnetic interactions with $N_{Fe-S-Fe}$ and $N_{Fe-X-Fe}$ given in parentheses for each group of BS states. Spin distributions (A, inset) show representative examples from each group used in calculations with various functionals and basis sets (C).

The nomenclature for the BS states was adapted from Ref. 17. Numerical results are available as supporting information.

Figure 3.
Three of the formal oxidation state distributions for the 2Fe^{II}-5Fe^{III} state, with subcluster M_s values indicated below. Calculated spin densities ρ_s(Fe) for [2Fe^{II}-5Fe^{III}-N^{3-}] are given on the right.
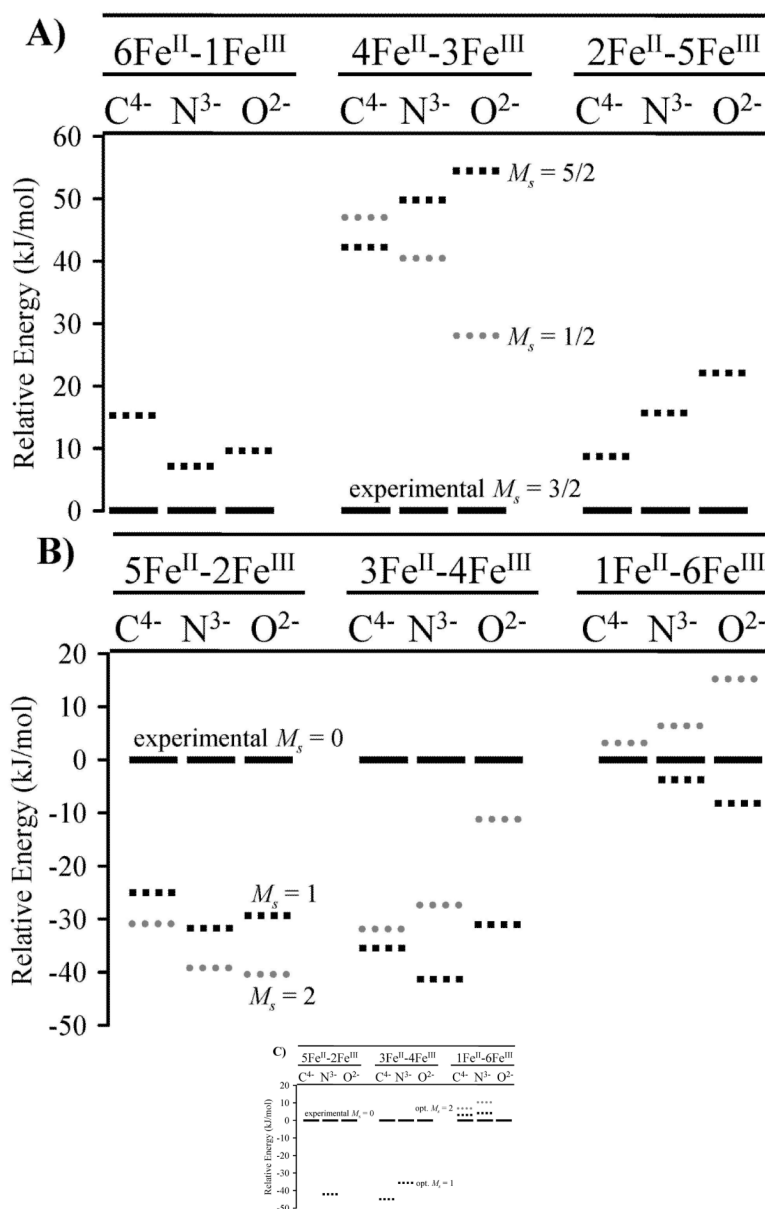
Figure 4.
Relative energies of (A) the $M_s = 1/2$ (dotted gray line) and 5/2 BS states (dotted black line) to the $M_s = 3/2$ ground BS state (solid black line) of FeMo-co^N, and the $M_s = 1$ (dotted gray line) and 2 BS states (dotted black line) relative to the $M_s = 0$ BS state (solid black line) of FeMo-co^{Ox} using the experimental crystal structure (B) and optimized geometries (C). Numerical results are available as supporting information.

Table 1

Interatomic distances in optimized FeMo-co^N for selected oxidation states. Experimental distances are given for the average of four FeMo-co structures from the crystal structure[2] along with those from two EXAFS studies.[6, 72] Superscripts (Fe) and (Mo) refer to the [4Fe-3S] and [Mo-3Fe-3S] subclusters, respectively; (b) denotes the bridging sulfides. HC(O$_{hydroxyl}$) refers to the deprotonated (O$^-$) or protonated (OH) hydroxyl group of the homocitrate ligand.

	calculated distances (Å)									experiment
	2Fe^{II}-5Fe^{III}-X				4Fe^{II}-3Fe^{III}-X					
X =	C^{4-}		N^{3-}		C^{4-}		N^{3-}		O^{2-}	Ref. 2, 6, 72
HC(O$_{hydroxyl}$)	O^-	OH	O^-	OH	O^-	OH	O^-	OH	O^-	O^-
S(Cys)-Fe	2.22	2.20	2.20	2.18	2.30	2.28	2.27	2.26	2.25	2.27
Fe-S$^{(Fe)}$	2.26	2.25	2.25	2.25	2.32	2.32	2.31	2.31	2.32	2.28
Fe⋯Fe$^{(Fe)}$	2.63	2.62	2.63	2.63	2.73	2.72	2.73	2.72	2.73	2.66
S$^{(Fe)}$-Fe$^{(Fe)}$	2.28	2.27	2.28	2.27	2.32	2.31	2.31	2.30	2.30	2.27
Fe$^{(Fe)}$-S$^{(b)}$	2.19	2.19	2.19	2.19	2.24	2.23	2.23	2.23	2.22	2.23
Fe$^{(Fe)}$⋯Fe$^{(Fe)}$	2.65	2.64	2.69	2.68	2.66	2.65	2.67	2.67	2.80	2.65
Fe$^{(Fe)}$-X	2.01	2.00	2.03	2.03	2.01	2.00	2.01	2.01	2.10	1.98
Fe$^{(Fe)}$⋯Fe$^{(Mo)}$	2.59	2.57	2.58	2.57	2.62	2.61	2.62	2.61	2.76	2.59
Fe$^{(Mo)}$⋯Fe$^{(Mo)}$	2.66	2.66	2.68	2.68	2.61	2.60	2.63	2.63	2.74	2.61
Fe$^{(Mo)}$-S$^{(b)}$	2.20	2.19	2.20	2.18	2.24	2.22	2.23	2.21	2.23	2.22
Fe$^{(Mo)}$-X	2.00	2.00	2.00	2.00	2.01	2.00	2.02	2.01	2.12	2.02
Fe$^{(Mo)}$⋯Mo	2.76	2.72	2.78	2.74	2.74	2.70	2.75	2.71	2.76	2.69
S$^{(Mo)}$-Fe$^{(Mo)}$	2.28	2.28	2.29	2.29	2.29	2.28	2.29	2.28	2.28	2.23
S$^{(Mo)}$-Mo	2.40	2.37	2.40	2.37	2.39	2.37	2.40	2.38	2.41	2.35
Mo-N(His)	2.25	2.22	2.24	2.21	2.26	2.24	2.26	2.22	2.24	2.30
Mo-O$_{carboxyl}$	2.12	2.11	2.10	2.08	2.16	2.16	2.14	2.13	2.11	2.18
Mo-O$_{hydroxyl}$	2.01	2.22	1.98	2.20	2.05	2.26	2.03	2.23	2.01	2.20
avg. Mo-O/N	2.13	2.19	2.11	2.16	2.16	2.22	2.14	2.19	2.12	2.23
Fe⋯Mo	7.02	6.94	7.02	6.95	7.17	7.11	7.17	7.10	7.22	7.00
avg. error	−0.01	−0.02	−0.01	−0.01	0.02	0.02	0.02	0.02	0.05	
RMS dev.	0.06	0.04	0.07	0.05	0.06	0.04	0.07	0.04	0.11	

	calculated distances (Å)								experiment
	2Fe^{II}-5Fe^{III}-X				4Fe^{II}-3Fe^{III}-X				Ref. 2, 6, 72
X =	C^{4-}		N^{3-}		C^{4-}		N^{3-}		O^{2-} O$^-$
HC(O$_{hydroxyl}$)	O$^-$	OH	O$^-$	OH	O$^-$	OH	O$^-$	OH	
core avg. error	0.01	0.00	0.02	0.01	0.03	0.02	0.02	0.03	0.07
core RMS dev.	0.04	0.03	0.05	0.04	0.04	0.03	0.03	0.04	0.09

Table 2

Effect of homocitrate and imidazole ligand protonation states on the optimized Mo···Fe and Mo-L distances (Å) in the [2Fe^{II}-5Fe^{III}-N^{3-}] state. O$_{carboxyl}$$^{(d)}$ and O$_{carboxyl}$$^{(p)}$ represent protonation at the distal and proximal O$_{carboxyl}$ center, respectively. The RMS deviations are given relative to the crystal structure.

homocitrate imidazole	deprotonated protonated	deprotonated deprotonated	HO$_{carboxyl}$$^{(d)}$ protonated	HO$_{carboxyl}$$^{(p)}$ protonated	HO$_{hydroxyl}$ protonated	XRD Ref. 2	EXAFS Ref. 6	EXAFS Ref. 72
Mo···Fe$^{(Mo)}$	2.78	2.80	2.77	2.77	2.74	2.69	2.70	2.68
Mo···S$^{(Mo)}$	2.40	2.41	2.38	2.38	2.37	2.34	2.37	2.34
Mo-N(His)	2.24	2.17	2.23	2.23	2.21	2.30	2.21^a	2.29
Mo-O$_{carboxyl}$	2.10	2.12	2.26	2.24	2.08	2.18	2.21^a	2.14
Mo-O$_{hydroxyl}$	1.98	1.98	1.99	2.01	2.20	2.20	2.21^a	2.31
Avg. Mo-O/N	2.11	2.09	2.16	2.16	2.16	2.22	2.21	2.25
RMS dev.	0.12	0.13	0.11	0.10	0.06			

^{a}Mo-O/N distances were reported only as an average, due to inherent difficulty in distinguishing between light atoms.

Table 3

Reduction potentials (in V) relative to the standard hydrogen electrode (SHE). Column "s.p." indicates the spin projection correction using the two spin system model. The contributions under $\Delta G°_{solute}$ reflect the difference between the zero-point energy (ZPE), enthalpy and entropy corrections to the reduced and oxidized solvated species as a result of structural optimizations. Reduction potentials were calculated from $\Delta\varepsilon_{SCF}^{s.p.}$, $\Delta G°_{solute}$ and $\Delta\Delta G°_{solvation}$, as described in Eqs. (1)-(3). The models labeled "+H" are the $O_{hydroxyl}$-protonated models. All numbers are given in V.

| model | gas phase[a] | | | solute corrections | | | | $\Delta\Delta G°_{solv}$ | | $E°$ vs. SHE |
	$\Delta\varepsilon_{SCF}$	s.p.	$\Delta\varepsilon_{SCF}^{s.p.}$	ΔZPE	$\Delta H°$	$T\Delta S°$	$\Delta G°$	$\Delta\Delta G_{elec}$	$\Delta\Delta G_{non}$	
$[6Fe^{II}\text{-}1Fe^{III}\text{-}N^{3-}]^{5-}$	-6.37							8.14	-0.02	-2.68
$[4Fe^{II}\text{-}3Fe^{III}\text{-}C^{4-}]^{4-}$	-4.96							7.79	-0.02	-1.62
$[4Fe^{II}\text{-}3Fe^{III}\text{-}C^{4-}\text{+H}]^{3-}$	-2.81							6.07	-0.03	-1.19
$[4Fe^{II}\text{-}3Fe^{III}\text{-}N^{3-}]^{3-}$	-2.33			-0.01	0.00	0.04	-0.04	6.00	-0.03	-0.83
$[4Fe^{II}\text{-}3Fe^{III}\text{-}N^{3-}\text{+H}]^{2-}$	0.30	-0.02	0.28	-0.02	-0.02	-0.09	0.05	3.78	-0.02	-0.34
$[4Fe^{II}\text{-}3Fe^{III}\text{-}O^{2-}]^{2-}$	0.77			-0.01	-0.04	-0.13	0.08	3.58	-0.04	-0.05
$[4Fe^{II}\text{-}3Fe^{III}\text{-}O^{2-}\text{+H}]^{1-}$	3.45			-0.01	-0.02	-0.06	0.03	1.31	-0.04	0.31
$[2Fe^{II}\text{-}5Fe^{III}\text{-}C^{4-}]^{2-}$	0.68	-0.03	0.65	0.06	-0.03	-0.12	0.15	3.66	-0.03	0.00
$[2Fe^{II}\text{-}5Fe^{III}\text{-}C^{4-}\text{+H}]^{1-}$	3.46	-0.04	3.43	0.04	0.00	-0.03	0.07	1.34	-0.03	0.38
$[2Fe^{II}\text{-}5Fe^{III}\text{-}N^{3-}]^{1-}$	3.81	-0.03	3.77	0.04	0.03	0.06	0.01	1.25	-0.01	0.59
experiment (Ref. 11)										-0.042

[a] *In vacuo* electronic energy $\langle\Psi(0)\,|\,\hat{H}\,|\,\Psi(0)\rangle$[50] with PCM-optimized geometry.

Table 4

Mulliken spin densities ($|\rho_S(\text{Fe})|$), quadrupole splittings ($|\Delta E_Q|$) and isomer shifts (δ) averaged over the Fe sites; hyperfine couplings of Fe (a^{test}) and X ($a(X)$); and RMS deviations of the individual site hyperfine couplings (a_i) for a series of oxidation states and compositions, where +H indicates O$_{\text{hydroxyl}}$-protonated models.

level of theory	model	δ_1 (mm s^{-1})[a]	δ_2 (mm s^{-1})[a]	δ_3 (mm s^{-1})[a]	$|\rho_S(\text{Fe})|$	$|\Delta E_Q|$ (mm s^{-1})	a^{test} (MHz)	RMS dev. a_i(MHz)	$a(X)$ (MHz)
BP86[b]	2Fe^{II}-5Fe^{III}-N^{3-}	0.41	0.29[c]	0.45	2.92	1.13	−25.1	4.2	1.1
	4Fe^{II}-3Fe^{III}-N^{3-}	0.53	0.38[c]	0.54	3.06	1.03	−27.3	5.6	−0.3
	6Fe^{II}-1Fe^{III}-N^{3-}	0.68	0.52[c]	0.66	2.98	0.95	−29.6	5.0	−0.3
	2Fe^{II}-5Fe^{III}-C^{4-}	0.35	0.24[c]	0.40	2.73	0.90	−24.3	3.5	3.7
	4Fe^{II}-3Fe^{III}-C^{4-}	0.48	0.34[c]	0.50	2.89	0.94	−25.1	4.7	−0.7
	4Fe^{II}-3Fe^{III}-O^{2-}	d		d	3.27	d	−29.5	6.8	d
	2Fe^{II}-5Fe^{III}-C^{4-}+H	0.32	0.22	0.38	2.68	0.86	−23.8	3.3	2.7
	4Fe^{II}-3Fe^{III}-C^{4-}+H	0.45	0.32[c]	0.48	2.85	0.93	−24.4	4.5	−1.0
	4Fe^{II}-3Fe^{III}-N^{3-}+H	0.51	0.45	0.52	3.03	0.97	−27.0	5.5	−0.4
B3LYP[b]	2Fe^{II}-5Fe^{III}-C^{4-}+H				3.42	1.16	−25.4	5.9	6.1
	4Fe^{II}-3Fe^{III}-N^{3-}+H				3.50	1.43	−31.8	8.0	−0.7
B(5HF)P86/ 6-311+G(d)	2Fe^{II}-5Fe^{III}-C^{4-}+H				2.44		−24.1	2.7	
	4Fe^{II}-3Fe^{III}-N^{3-}+H				2.77		−25.1	4.5	
	Exp	0.41[e]		0.41[e]		0.69[e]	−17.9[e]		< 0.07[f]

[a] Subscripts refer to the methods employing a training data set with (1) crystal structures, (2) BP86/STO-TZP optimized structures, or (3) crystal structures without outliers.

[b] SDD-VTZ(d) basis set for $|\rho_S(\text{Fe})|$ and a^{test}; STO-TZP for $|\Delta E_Q|$, $a(X)$ and δ.

[c] Estimated based on range of δ for [2Fe^{II}-5Fe^{III}-C^{4-}+H].

[d] Calculations did not converge.

[e] Ref. 15

[f] Ref. 25

Table 5

Magnetic, electronic, geometric, and energetic preference for oxidation states of the iron centers and composition of the interstitial ligand. $HC(O^-_{hydroxyl})$ and $HC(HO_{hydroxyl})$ indicate the deprotonated and protonated states of homocitrate, respectively.

criterion	oxidation state	interstitial atom	
		$HC(O^-_{hydroxyl})$	$HC(HO_{hydroxyl})$
resting $S_t = 3/2$	no preference	no preference	no preference[a]
oxidized $S_t = 0$	Mo^{IV}-$2Fe^{II}$-$5Fe^{III}$	C^{4-}, N^{3-}	C^{4-a}, N^{3-a}
geometry	Mo^{IV}-$2Fe^{II}$-$5Fe^{III}$	C^{4-}, N^{3-}	C^{4-}
	Mo^{IV}-$4Fe^{II}$-$3Fe^{III}$		C^{4-}, N^{3-}
charge	Mo^{IV}-$2Fe^{II}$-$5Fe^{III}$	N^{3-}	C^{4-}
	Mo^{IV}-$4Fe^{II}$-$3Fe^{III}$		O^{2-}
reduction potential	Mo^{IV}-$2Fe^{II}$-$5Fe^{III}$	C^{4-}	C^{4-}
	Mo^{IV}-$4Fe^{II}$-$3Fe^{III}$	O^{2-}	N^{3-}, O^{2-}
isomer shift (all)	Mo^{IV}-$2Fe^{II}$-$5Fe^{III}$	C^{4-}, N^{3-}	C^{4-}, N^{3-b}
	Mo^{IV}-$4Fe^{II}$-$3Fe^{III}$	C^{4-}, N^{3-}	C^{4-}, N^{3-}
isomer shift (δ_3)	Mo^{IV}-$2Fe^{II}$-$5Fe^{III}$	C^{4-}, N^{3-}	C^{4-}, N^{3-b}
quadrupole splitting	Mo^{IV}-$2Fe^{II}$-$5Fe^{III}$	C^{4-}	C^{4-}
	Mo^{IV}-$4Fe^{II}$-$3Fe^{III}$	C^{4-}	C^{4-}, N^{3-}
	Mo^{IV}-$6Fe^{II}$-$1Fe^{III}$	N^{3-}	N^{3-b}
Fe hyperfine coupling	Mo^{IV}-$2Fe^{II}$-$5Fe^{III}$	C^{4-}	C^{4-}
X hyperfine coupling	no preference	no preference	no preference

[a] Estimated based on results for deprotonated models. The $S_t = 0$ and 1 states of [$2Fe^{II}$-$5Fe^{III}$-C^{4-}+H] were tested and the results were consistent with the deprotonated case.

[b] [$2Fe^{II}$-$5Fe^{III}$-N^{3-}+H] and [$6Fe^{II}$-$1Fe^{III}$-N^{3-}+H] results estimated.